CMB power spectrum estimation using noncircular beams

Sanjit Mitra,* Anand S. Sengupta,† and Tarun Souradeep‡

Inter-University Centre for Astronomy and Astrophysics, Post Bag 4, Ganeshkhind, Pune 411007, India
(Received 24 May 2004; published 11 November 2004)

The measurements of the angular power spectrum of the Cosmic Microwave Background (CMB) anisotropy have proved crucial to the emergence of cosmology as a precision science in recent years. In this remarkable data rich period, the limitations to precision now arise from the inability to account for finer systematic effects in data analysis. The noncircularity of the experimental beam has become progressively important as CMB experiments strive to attain higher angular resolution and sensitivity. We present an analytic framework for studying the leading order effects of a noncircular beam on the CMB power spectrum estimation. We consider a noncircular beam of fixed shape but variable orientation. We compute the bias in the pseudo-C_l power spectrum estimator and then construct an unbiased estimator using the bias matrix. The covariance matrix of the unbiased estimator is computed for smooth, noncircular beams. Quantitative results are shown for CMB maps made by a *hypothetical* experiment with a noncircular beam comparable to our fits to the Wilkinson Microwave Anisotropy Probe (WMAP) beam maps described in the appendix and uses a *toy* scan strategy. We find that significant effects on CMB power spectrum can arise due to noncircular beam on multipoles comparable to, and beyond, the inverse average beamwidth where the pseudo-C_l approach may be the method of choice due to computational limitations of analyzing the large data sets from current and near future CMB experiments.

PACS numbers: 98.70.Vc, 95.75.Pq, 98.80.Es

I. INTRODUCTION

A golden decade of measurements of the cosmic microwave background anisotropy has ushered in an era of precision cosmology. The theory of primary Cosmic Microwave Background (CMB) anisotropy is well-developed and the past decade has seen a veritable flood of data [1–3]. Increasingly sensitive, high resolution, "full" sky measurements from space missions, such as, the ongoing Wilkinson Microwave Anisotropy Probe (WMAP) and the upcoming Planck surveyor pose a stiff challenge for current analysis techniques to realize the full potential of precise determination of cosmological parameters. As experiments improve in sensitivity, the inadequacy in modeling the observational reality start to limit the returns from these experiments.

A Gaussian model of CMB anisotropy $\Delta T(\hat{\mathbf{q}})$ is completely specified by its angular two-point correlation function. In standard cosmology, CMB anisotropy is expected to be statistically isotropic. In spherical harmonic space, where $\Delta T(\hat{\mathbf{q}}) = \sum_{lm} a_{lm} Y_{lm}(\hat{\mathbf{q}})$, this translates to a diagonal $\langle a_{lm} a_{l'm'}^* \rangle = C_l \delta_{ll'} \delta_{mm'}$ where C_l, the widely used angular power spectrum of CMB anisotropy is a complete description of a Gaussian CMB anisotropy. Observationally, the angular power spectrum being a simple, robust point statistics is the obvious first target for cosmological observations. Theoretically, the C_l are deemed all important since the simplest inflation models predict a Gaussian CMB anisotropy. In this case, the power spectrum provides an economical description of the CMB anisotropy allowing easy comparison to observations.

Accurate estimation of C_l is arguably the foremost concern of most CMB experiments. The extensive literature on this topic has been summarized in a recent article [4]. For Gaussian, statistically isotropic CMB sky, the C_l that correspond to covariance that maximize the multivariate Gaussian PDF of the temperature map, $\Delta T(\hat{\mathbf{q}})$, is the Maximum Likelihood (ML) solution. Different ML estimators have been proposed and implemented on CMB data of small and modest size [5–10]. While it is desirable to use optimal estimators of C_l that obtain (or iterate toward) the ML solution for the given data, these methods usually are limited by the computational expense of matrix inversion that scales as N_d^3 with data size N_d [11,12]. Various strategies for speeding up ML estimation have been proposed, such as, exploiting the symmetries of the scan strategy [13], using hierarchical decomposition [14], iterative multigrid method [15], etc., Variants employing linear combinations of $\Delta T(\hat{\mathbf{q}})$ such as a_{lm} on a set of rings in the sky can alleviate the computational demands in special cases [16,17]. Other promising exact power estimation methods have been recently proposed [18–20].

However there also exist computationally rapid, suboptimal estimators of C_l. Exploiting the fast spherical harmonic transform ($\sim N_d^{3/2}$), it is possible to estimate the angular power spectrum $C_l = \langle |a_{lm}|^2 \rangle / (2l + 1)$ rapidly [21,22]. This is commonly referred to as the pseudo-C_l method [23]. (Analogous approach employing fast estimation of the correlation function $C(\hat{\mathbf{q}} \cdot \hat{\mathbf{q}}')$ have

*sanjit@iucaa.ernet.in
†anandss@iucaa.ernet.in
‡tarun@iucaa.ernet.in

70 103002-1

also been explored [24,25].) It has been recently argued that the need for optimal estimators may have been overemphasized since they are computationally prohibitive at large l. Suboptimal estimators are computationally tractable and tend to be nearly optimal in the relevant high l regime. Moreover, already the data size of the current sensitive, high resolution, "full sky" CMB experiments such as WMAP have compelled the use of suboptimal pseudo-C_l related methods [26,27]. On the other hand, optimal ML estimators can readily incorporate and account for various systematic effects, such as nonuniform sky coverage, noise correlations, and beam asymmetries.

In the years after the COBE-DMR observations [28], more sensitive measurements at higher resolution but with limited sky coverage were made by a number of experiments[1]. The effect of incomplete (more generally, nonuniform) sky coverage on the sampling statistics of C_l was the dominant concern of these experiments such as the ground based experiment TOCO [29], DASI [30], CBI [31], ACBAR [32], and balloon-based experiments BOOMERang [33], MAXIMA, [34,35] and Archeops [36]. Comprehensive analyses have been carried out to tackle this problem. For example, the basic semianalytic framework developed [23] was subsequently implemented as a fast, efficient scheme for the analysis of the BOOMERang experiment [37]. While the nonuniform sky coverage has been addressed in the pseudo-C_l method, the other effects remain to be incorporated.

In this paper, we initiate a similar line of research to address a more contemporary issue that has gained relative importance in the post WMAP [26] (and pre-Planck) era of CMB anisotropy measurement with full sky coverage. It has been usual in CMB data analysis to assume the experimental beam response to be circularly symmetric around the pointing direction. However, any real beam response function has deviations from circular symmetry. Even the main lobe of the beam response of experiments are generically noncircular (nonaxisymmetric) since detectors have to be placed off-axis on the focal plane. (Side lobes and stray light contamination add to the breakdown of this assumption). For high sensitive experiments, the systematic errors arising from the beam noncircularity become progressively more important. Recent CMB experiments such as ARCHEOPS, MAXIMA, WMAP have significantly noncircular beams. Future experiments like the Planck Surveyor are expected to be even more seriously affected by noncircular beams.

Dropping the circular beam assumption leads to major complications at every stage of the data analysis pipeline. The extent to which the noncircularity affects the step of going from the time stream data to sky map is very sensitive to the scan strategy. The beam now has an orientation with respect to the scan path that can potentially vary along the path. This implies that the beam function is inherently time dependent and difficult to deconvolve. Even after a sky map is made, the noncircularity of the effective beam affects the estimation of the angular power spectrum, C_l, by coupling the l modes, typically, on scales beyond the inverse angular beamwidth.

Barring few exceptions (eg., [38]), the noncircularity of beam patterns in CMB experiments has been addressed in limited context. When it has not been totally ignored, one has measured with numerical simulations the biasing effect on the power spectrum of CMB anisotropies of neglecting the noncircularity of the beams in the data analysis chain (see, e.g., MAXIMA [35,39], Archeops [36,40]). This approach only deals with the diagonal part of the matrix relating the observed power spectrum to the underlying power spectrum, so it does not fully describe the effect of the beam complexity on the CMB statistics. An integrated approach to account for the systematic effect of a noncircular beam has not yet been developed.

In this initial work we skip over the issues related to map-making and focus on the CMB power spectrum estimation from a CMB sky map made with an effective beam that is noncircular. Mild deviations from circularity can be addressed by a perturbation approach [41,42]. Besides providing an elegant analytic formalism, the approach has lead to rapid methods for computing the window functions for CMB experiments [43]. In this work the effect of beam noncircularity on the estimation of CMB power spectrum is studied analytically using this perturbation approach.

We present a brief primer on the connection between CMB power spectrum and the experimental window functions in Sec. II. The section is designed to keep the paper self-contained and also serves to set the notation for the rest of the paper. In section II B, we briefly review the perturbation approach for computing the window functions for CMB experiments with noncircular beam [41] and also define the elliptical Gaussian beam and its spherical transform. The bias matrix accounting for the noncircularity of the beam for the pseudo-C_l estimator of CMB anisotropy is derived and discussed in Sec. III. The error-covariance for the unbiased estimator is derived in Sec. III. We conclude with a discussion of the results in Sec. IV. An interesting exercise of fitting the WMAP beam maps with an elliptical Gaussian beam profile is presented in an appendix A. Details of the steps leading to our analytical results are given in Appendix B.

II. WINDOW FUNCTIONS OF CMB EXPERIMENTS: A BRIEF PRIMER

Conventionally, the CMB temperature, $\Delta T(\hat{\mathbf{q}})$, is expressed as a function of angular position, $\hat{\mathbf{q}} \equiv (\theta, \phi)$, on

---

[1]For a compendium of links to experiments refer to, e.g. http://www.mpa-garching.mpg.de/~banday/CMB.html.

the sky via the spherical harmonic decomposition,

$$\Delta T(\hat{\mathbf{q}}) = \sum_{l=0}^{\infty} \sum_{m=-l}^{l} a_{lm} Y_{lm}(\hat{\mathbf{q}}). \qquad (1)$$

In an idealized noise-free, CMB anisotropy sky map $\Delta T(\hat{\mathbf{q}})$ made with infinitely high resolution, the angular power spectrum is given by

$$C_l \equiv \frac{1}{2l+1} \sum_{m=-l}^{l} \langle |a_{lm}|^2 \rangle, \qquad (2)$$

where

$$a_{lm} \equiv \int d\Omega_{\hat{\mathbf{q}}} Y_{lm}^*(\hat{\mathbf{q}}) \Delta T(\hat{\mathbf{q}}) \qquad (3)$$

are the spherical harmonic transforms of the temperature deviation field $\Delta T(\hat{\mathbf{q}})$. We introduce the scaled power spectrum $\mathcal{C}_l \equiv [l(l+1)/2\pi]C_l$, that measures the power per logarithmic interval of angular scale, l. Eliminating a_{lm}, we may write,

$$C_l = \frac{l(l+1)}{8\pi^2} \int d\Omega_{\hat{\mathbf{q}}_1} \int d\Omega_{\hat{\mathbf{q}}_2} \langle \Delta T(\hat{\mathbf{q}}_1) \Delta T(\hat{\mathbf{q}}_2) \rangle$$
$$\times P_l(\hat{\mathbf{q}}_1 \cdot \hat{\mathbf{q}}_2), \qquad (4)$$

where we have made use of the expansion of Legendre Polynomials

$$P_l(\hat{\mathbf{q}}_1 \cdot \hat{\mathbf{q}}_2) = \frac{4\pi}{2l+1} \sum_{m=-l}^{l} Y_{lm}^*(\hat{\mathbf{q}}_1) Y_{lm}(\hat{\mathbf{q}}_2). \qquad (5)$$

If we assume the isotropy of the CMB sky, $\langle \Delta T(\hat{\mathbf{q}}_1) \Delta T(\hat{\mathbf{q}}_2) \rangle$ should depend only on $\hat{\mathbf{q}}_1 \cdot \hat{\mathbf{q}}_2$. Therefore, we can use Legendre expansion to show that,

$$\langle \Delta T(\hat{\mathbf{q}}_1) \Delta T(\hat{\mathbf{q}}_2) \rangle = \sum_{l=0}^{\infty} \frac{2l+1}{2l(l+1)} \mathcal{C}_l P_l(\hat{\mathbf{q}}_1 \cdot \hat{\mathbf{q}}_2). \qquad (6)$$

All CMB anisotropy experiments measure differences in CMB temperature at different locations on the sky. A step of map-making is required to derive the above temperature anisotropy map at each point on the sky. Since this is a linear operation, the correlation function of the measured quantity for a given scanning or modulation strategy can always be expressed as linear sum of "elementary" correlations of the temperature given in Eq. (6).

Typically, a CMB anisotropy experiment probes a range of angular scales characterized by a *window* function $W_l(\hat{\mathbf{q}}, \hat{\mathbf{q}}')$. The window depends both on the scanning strategy as well as the angular resolution and response of the experiment. However, it is neater to logically separate these two effects by expressing the window $W_l(\hat{\mathbf{q}}, \hat{\mathbf{q}}')$ as a sum of elementary window function of the CMB anisotropy at each point of the map [41]. In this work, we only deal with these elementary window functions. For a given scanning/modulation strategy, our results can be readily

generalized using the representation of the window function as sum over elementary window functions (see, e.g., [41,43]). Although the quantitative results we present in this paper refer to a scan strategy where each pixel is visited by the beam only once, this is not a limitation of our approach. If pixels are multiply visited by the beam with different orientations, the correlation function still can be expressed as a sum over appropriate elementary window functions for which all the results we describe in this paper hold.

A. Window function for circular beams

Because of finite resolution of the instruments, the "measured" temperature difference $\widetilde{\Delta T}(\hat{\mathbf{q}})$ along the direction $\hat{\mathbf{q}}$ in response to the CMB anisotropy signal $\Delta T(\hat{\mathbf{q}}')$ is given by

$$\widetilde{\Delta T}(\hat{\mathbf{q}}) = \int d\Omega_{\hat{\mathbf{q}}'} B(\hat{\mathbf{q}}, \hat{\mathbf{q}}') \Delta T(\hat{\mathbf{q}}') \qquad (7)$$

where the experimental "Beam" response function $B(\hat{\mathbf{q}}, \hat{\mathbf{q}}')$ describes the sensitivity of the measuring instrument at different angles around the pointing direction. There is an additional contribution from instrumental noise denoted by $n(\hat{\mathbf{q}})$ which we shall introduce later into our final results.

The two-point correlation function for a statistical isotropic CMB anisotropy signal is

$$C(\hat{\mathbf{q}}, \hat{\mathbf{q}}') = \langle \widetilde{\Delta T}(\hat{\mathbf{q}}) \widetilde{\Delta T}(\hat{\mathbf{q}}') \rangle = \sum_{l=0}^{\infty} \frac{(2l+1)}{4\pi} C_l W_l(\hat{\mathbf{q}}, \hat{\mathbf{q}}'), \qquad (8)$$

where C_l is the angular spectrum of CMB anisotropy signal and the window function

$$W_l(\hat{\mathbf{q}}_1, \hat{\mathbf{q}}_2) \equiv \int d\Omega_{\hat{\mathbf{q}}} \int d\Omega_{\hat{\mathbf{q}}'} B(\hat{\mathbf{q}}_1, \hat{\mathbf{q}}) B(\hat{\mathbf{q}}_2, \hat{\mathbf{q}}') P_l(\hat{\mathbf{q}} \cdot \hat{\mathbf{q}}'), \qquad (9)$$

encodes the effect of finite resolution through the beam function.

For some experiments, the beam function may be assumed to be circularly symmetric about the pointing direction, i.e., $B(\hat{\mathbf{q}}, \hat{\mathbf{q}}') \equiv B(\hat{\mathbf{q}} \cdot \hat{\mathbf{q}}')$ without significantly affecting the results of the analysis. In any case, this assumption allows a great simplification since the beam function can then be represented by an expansion in Legendre polynomials as

$$B(\hat{\mathbf{q}} \cdot \hat{\mathbf{q}}') = \frac{1}{4\pi} \sum_{l=0}^{\infty} (2l+1) B_l P_l(\hat{\mathbf{q}} \cdot \hat{\mathbf{q}}'). \qquad (10)$$

Consequently, it is straightforward to derive the well-known simple expression

$$W_l(\hat{\mathbf{q}}, \hat{\mathbf{q}}') = B_l^2 P_l(\hat{\mathbf{q}} \cdot \hat{\mathbf{q}}'), \qquad (11)$$

for a circularly symmetric beam function.

B. Window function for noncircular beams

While some experiments may have circularly symmetric beam functions, most experimental beams are noncircular to some extent. The effect of noncircularity of the beam has become progressively more relevant for experiments with higher sensitivity and angular resolution. The most general beam response function can be represented as

$$B(\hat{\mathbf{z}}, \hat{\mathbf{q}}) = \sum_{l=0}^{\infty} \sum_{m=-l}^{l} b_{lm}(\hat{\mathbf{z}}) Y_{lm}(\hat{\mathbf{q}}) \qquad (12)$$

by a spherical harmonic expansion when pointing along $\hat{\mathbf{z}}$ axis ("North pole" in some given astronomical coordinate system). In case of circularly symmetric beams, the real coefficients $B_l = \sqrt{4\pi/(2l+1)}b_{l0}$.

For mild deviations, the noncircularity of the beams can be parametrized by a set of *small* quantities $\beta_{lm} \equiv b_{lm}/b_{l0}$—the Beam Distortion Parameters (BDP). The smoothness of the beam response implies that at any multipole l, the coefficients β_{lm} decrease sufficiently rapidly with increasing $|m|$. In addition, for the rest of paper we assume that the beam function has reflection symmetry about two orthogonal axes on the (locally flat) beam plane, which ensures that the coefficients $b_{lm}(\hat{\mathbf{z}})$ are real and zero for *odd* values of m. An example of a noncircular beam with such symmetries is the elliptical Gaussian beam. A brief mathematical description of such beams can be found later in this section. In order to verify our analytical results, we have used the elliptical Gaussian beam as a model of noncircular beam. However, our analytic results would apply to a general form of noncircular beam (as long as β_{l1} is zero or subdominant to β_{l2}).

In order to find an expression for window function in terms of the β_{lm} and B_l, we follow the approach in [41]. The beam transforms for an arbitrary pointing direction $\hat{\mathbf{q}}$ may be expressed as,

$$b_{lm}(\hat{\mathbf{q}}) = \sum_{m'=-l}^{l} b_{lm'}(\hat{\mathbf{z}}) D_{mm'}^l[\hat{\mathbf{q}}, \rho(\hat{\mathbf{q}})], \qquad (13)$$

where $D_{mm'}^l(\hat{\mathbf{q}}, \rho) \equiv D_{mm'}^l(\phi, \theta, \rho)$ are the Wigner-D functions given in terms of the Euler angles describing the rotation that carries the pointing direction $\hat{\mathbf{q}}$ to $\hat{\mathbf{z}}$-axis, as illustrated in Fig. 1. The third angle $\rho(\hat{\mathbf{q}})$ measures the angle by which the beam has rotated about the new pointing direction, when the pointing direction moves from $\hat{\mathbf{z}}$ to $\hat{\mathbf{q}}$.[2] Inserting the spherical transform of the

---

[2] Hereafter, for brevity of notation, absence of the pointing direction argument to b_{lm} or β_{lm} will imply a beam pointed along the $\hat{\mathbf{z}}$ axis.
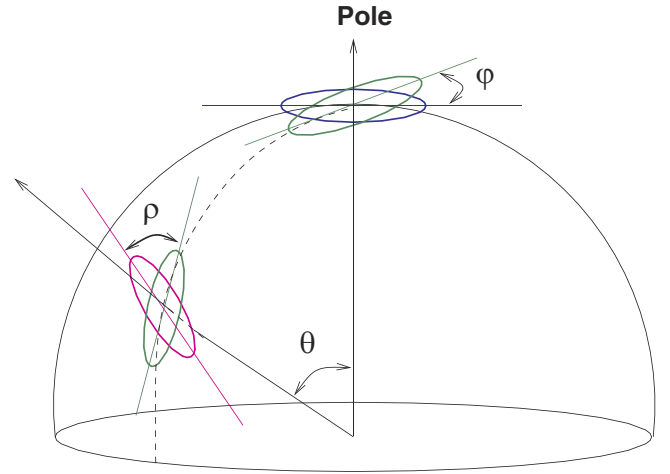

Pole

FIG. 1 (color online). The figure illustrates that a beam pointed in an arbitrary direction $\hat{\mathbf{q}} = (\theta, \phi)$, with an orientation given by the angle $\rho(\hat{\mathbf{q}})$ can always be rotated to point along $\hat{\mathbf{z}}$ oriented with $\rho(\hat{\mathbf{z}}) = 0$. The Euler angles of this rotation are clearly seen to be (θ, ϕ, ρ). Consequently, the beam transforms are related through Wigner rotation matrices corresponding to the same rotation.

beam in Eq. (13) into Eq. (9) we can write the window function as

$$W_l(\hat{\mathbf{q}}_1, \hat{\mathbf{q}}_2) = \frac{4\pi}{2l+1} \sum_{m=-l}^{l} b_{lm}^*(\hat{\mathbf{q}}_1) b_{lm}(\hat{\mathbf{q}}_2) \qquad (14)$$

$$= B_l^2 \sum_{m_1=-l}^{l} \sum_{m_2=-l}^{l} \beta_{lm_1}^* \beta_{lm_2} \sum_{m=-l}^{l} D_{mm_1}^{l*}[\hat{\mathbf{q}}_1, \rho(\hat{\mathbf{q}}_1)]$$
$$\times D_{mm_2}^l[\hat{\mathbf{q}}_2, \rho(\hat{\mathbf{q}}_2)] \qquad (15)$$

solely in terms of the circular component of the beam function B_l and noncircular parts encoded in the BDP's, β_{lm}. As pointed out in [41], the window function expressed in the form of Eq. (15) has an obvious expansion in perturbation series in β_{lm} retaining only the lowest values of $|m_1|$ and $|m_2|$. In this paper, we adopt this perturbation approach to evaluate the leading order correction to power spectrum estimation arising due to mild deviations of the beam from circular symmetry.

For numerical evaluation it is advantageous to use the summation formula of Wigner-D to combine the product of the two Wigner-D functions in Eq. (15) into a single one as [41]

$$W_l(\hat{\mathbf{q}}_1, \hat{\mathbf{q}}_2) = \frac{4\pi}{2l+1} \sum_{m'=-l}^{l} \sum_{m''=-l}^{l} [b_{lm'}(\hat{\mathbf{z}})]^* b_{lm''}(\hat{\mathbf{z}})$$
$$\times D_{m'm''}^l(\alpha - \rho_1, \gamma, \beta + \rho_2), \qquad (16)$$

where

$$\cos\gamma = \hat{\mathbf{q}}_1 \cdot \hat{\mathbf{q}}_2$$
$$\cot\alpha = -\cos\theta_1\cot(\phi_1 - \phi_2) + \sin\theta_1\cot\theta_2\csc(\phi_1 - \phi_2)$$
$$\cot\beta = -\cos\theta_2\cot(\phi_1 - \phi_2) + \cot\theta_1\sin\theta_2\csc(\phi_1 - \phi_2).$$

$$(17)$$

$$W_l(\hat{\mathbf{q}}_1, \hat{\mathbf{q}}_2) = \frac{4\pi}{2l+1}\{[b_{l0}(\hat{\mathbf{z}})]^2 d_{00}^l(\gamma) + 2b_{l0}(\hat{\mathbf{z}})b_{l2}(\hat{\mathbf{z}})[\cos(2(\alpha - \rho_1)) + \cos(2(\beta + \rho_2))]d_{02}^l(\gamma) + 2[b_{l2}(\hat{\mathbf{z}})]^2$$
$$\times [\cos(2(\alpha + \beta + \rho_2 - \rho_1))d_{22}^l(\gamma) + (-1)^{-l}\cos(2(\alpha - \beta - \rho_1 - \rho_2)))d_{22}^l(\pi - \gamma)] + 2b_{l0}(\hat{\mathbf{z}})b_{l4}(\hat{\mathbf{z}})$$
$$\times [\cos(4(\alpha - \rho_1)) + \cos(4(\beta + \rho_2))]d_{04}^l(\gamma) + \ldots\}. \qquad (18)$$

can be readily evaluated using recurrence relations similar to that of Legendre function. In the above we have restricted to the common situation of beam functions with reflection symmetry (β_{lm} are real and $\beta_{lm} = 0$ for odd m) such as the elliptic Gaussian beam described next.

An elliptic Gaussian beam profile, pointed along the $\hat{\mathbf{z}}$-axis is expressed in terms of the spherical polar coordinates about the pointing direction as follows [41]

$$B(\hat{\mathbf{z}}, \hat{\mathbf{q}}) = \frac{1}{2\pi\sigma_1\sigma_2} \exp\left[-\frac{\theta^2}{2\sigma^2(\phi)}\right], \qquad (19)$$

where the "beamwidth" $\sigma(\phi) \equiv [\sigma_1^2/(1 + \epsilon\sin^2\phi)]^{1/2}$ and the "noncircularity parameter" $\epsilon \equiv (\sigma_1^2/\sigma_2^2 - 1)$ are given in terms of σ_1 and σ_2—the Gaussian widths along the semimajor and semiminor axis, respectively. However, we characterize an elliptical beam using two different parameters: eccentricity $e \equiv \sqrt{1 - \sigma_2^2/\sigma_1^2}$ and the size parameter $\theta_{1/2}$, the FWHM of a circular beam of equal "area"[3].

For elliptical Gaussian beams the spherical harmonic transform is available in the closed analytical form

$$b_{lm} = \left[\frac{2l+1}{4\pi}\frac{(l+m)!}{(l-m)!}\right]^{\frac{1}{2}}$$
$$\times (l+1/2)^{-m}I_{m/2}\left[\frac{(l+1/2)^2\sigma_1^2 e^2}{4}\right]$$
$$\times \exp\left[-\frac{(l+1/2)^2\sigma_1^2}{2}\left\{1 - \frac{e^2}{2}\right\}\right], \qquad (20)$$

where $I_\nu(x)$ is the modified Bessel function [41,44]. Note, in the above equation we have used eccentricity e instead of the noncircularity parameter $\epsilon = e^2/(1 - e^2)$ used in [41]. (Please see Table I for the various definitions and characterizations of elliptical beams.)

___
[3]By area we mean the area enclosed by the curve whose each point corresponds to the Half Maximum of the Gaussian profile. We can show that, $\theta_{1/2}$(in degrees) $= (180/\pi) \times \sqrt{8\ln 2}\bar{\sigma}$, where $\bar{\sigma}^2 \equiv \sigma_1\sigma_2$ is proportional to the area of the beam.

For large values of l it is computationally expensive to evaluate the entire m' and m'' sum in Eq. (16). However, for a smooth, mildly noncircular beam function, restricting the summation to a few low values of m' and m'' results in a good approximation. The leading order terms in the perturbation [41]

Figure 2 shows one of the WMAP beams as an example of a distinctly noncircular beam (see isocontours in the top panel) that can be efficiently handled by the leading order term in the perturbation approach (see the bottom panel). Details of the exercise of fitting elliptical Gaussian beam profile to the WMAP beam maps is given in appendix A.

III. BIAS MATRIX

Given the observed temperature fluctuations $\widetilde{\Delta T}(\hat{\mathbf{q}})$, a naive estimator for the angular power spectrum based on Eq. (2) is given by

$$\widetilde{C}_l \equiv \frac{l(l+1)}{2\pi}\frac{1}{2l+1}\sum_{m=-l}^{l}|\tilde{a}_{lm}|^2, \qquad (21)$$

where

$$\tilde{a}_{lm} \equiv \int d\Omega_{\hat{\mathbf{q}}} Y_{lm}^*(\hat{\mathbf{q}})\widetilde{\Delta T}(\hat{\mathbf{q}})w(\hat{\mathbf{q}}) \qquad (22)$$

are the coefficients of the spherical harmonic transform of the CMB anisotropy map [21,22]. The weight function $w(\hat{\mathbf{q}})$ accounts for nonuniform/incomplete sky coverage and also provides a handle to weigh the data "optimally". Without the inconsequential $l(l + 1)$ scaling, this naive estimator is referred to as the pseudo-C_l in recent literature [23]. The "pseudo" refers to fact that the estimated C_l is biased. Moreover, this is a suboptimal estimator of the

TABLE I. In literature, the elliptical beams have been described by several parameters which can all be expressed in terms of the Gaussian widths along the semimajor (σ_1) and the semiminor (σ_2) axes of the ellipse. We have used these parameters at several places in the paper.

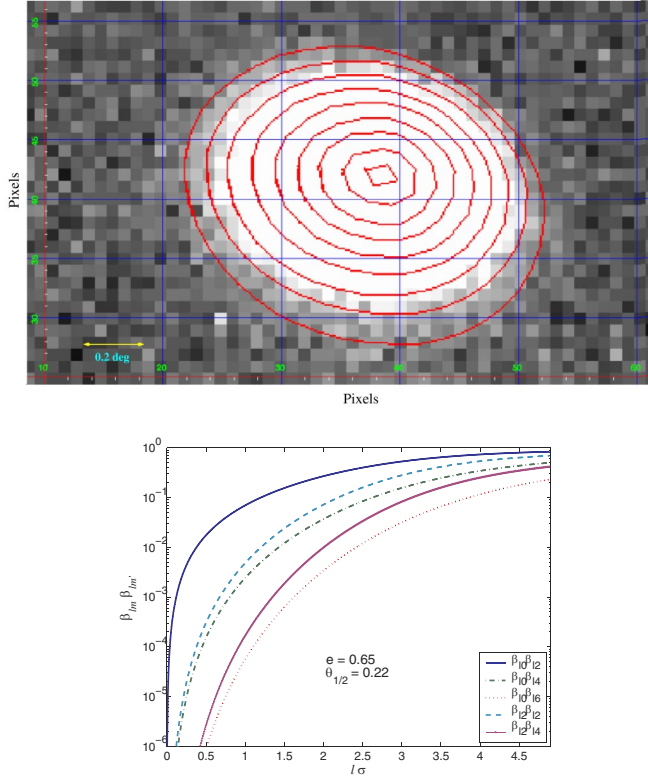| Parameter	Symbol	Expression
Eccentricity	e	$\sqrt{1 - \frac{\sigma_2^2}{\sigma_1^2}}$
Noncircularity Parameter	ϵ	$\frac{\sigma_1^2}{\sigma_2^2} - 1$
Ellipticity	$\bar{\epsilon}$	$1 - \frac{\sigma_2}{\sigma_1}$

FIG. 2 (color online). The top panel shows the WMAP Q1 (A side) beam map overlaid with IRAF fitted ellipses over iso-intensity contours. More details are in Appendix A. On the bottom panel, we plot the product of beam distortion parameters for the elliptic Gaussian fit to the WMAP-Q1 beam versus multipole corresponding to the different order of the perturbation expansion of a window function for a noncircular beam. Note that the effect kicks in at $l\bar{\sigma} \sim 1$.

power spectrum. This naive power spectrum estimate has to be corrected for observational effects such as the instrumental noise contribution, beam resolution, incomplete/nonuniform sky coverage. Nevertheless, the pseudo-C_l method is a computationally fast and economical approach and is currently a method of choice for the recent large CMB anisotropy data sets (at least for large l within the hybrid schemes [4]).

Faced with the computational challenges of large data sets, an approach that has been adopted is to compute the pseudo-C_l's from the CMB observations and then correct for the observational effects. The true C_l spectrum is linearly related

$$\langle \tilde{C}_l \rangle = \sum_{l'} A_{ll'} C_{l'} \tag{23}$$

to the pseudo-C_l through a *bias* matrix $A_{ll'}$. Similar bias matrices arising due to the effect of nonuniform sky coverage, instrumental noise have been studied [23,37]. In this paper, we compute the $A_{ll'}$ for noncircular beam and give explicit analytical results for the leading order terms for nonrotating beams.

The pseudo-C_l estimator in Eq. (21) can be expressed as

$$\tilde{C}_l \equiv \frac{l(l+1)}{8\pi^2}$$
$$\times \int d\Omega_{\hat{\mathbf{q}}_1} \int d\Omega_{\hat{\mathbf{q}}_2} w(\hat{\mathbf{q}}_1) w(\hat{\mathbf{q}}_2) \widetilde{\Delta T}(\hat{\mathbf{q}}_1) \widetilde{\Delta T}(\hat{\mathbf{q}}_2)$$
$$\times P_l(\hat{\mathbf{q}}_1 \cdot \hat{\mathbf{q}}_2). \tag{24}$$

The ensemble expectation value of the pseudo-C_l power spectrum estimator is

$$\langle \tilde{C}_l \rangle = \frac{l(l+1)}{8\pi^2} \int d\Omega_{\hat{\mathbf{q}}_1} \int d\Omega_{\hat{\mathbf{q}}_2} w(\hat{\mathbf{q}}_1) w(\hat{\mathbf{q}}_2)$$
$$\times \sum_{l'} \frac{2l'+1}{2l'(l'+1)} C_{l'} P_l(\hat{\mathbf{q}}_1 \cdot \hat{\mathbf{q}}_2)$$
$$\times \int d\Omega_{\hat{\mathbf{q}}} \int d\Omega_{\hat{\mathbf{q}}'} B(\hat{\mathbf{q}}_1, \hat{\mathbf{q}}) B(\hat{\mathbf{q}}_2, \hat{\mathbf{q}}') P_{l'}(\hat{\mathbf{q}} \cdot \hat{\mathbf{q}}'). \tag{25}$$

Recalling the definition of a window function in Eq. (9), the most general form of the bias matrix

$$A_{ll'} = \frac{2l'+1}{16\pi^2} \frac{l(l+1)}{l'(l'+1)} \int d\Omega_{\hat{\mathbf{q}}_1}$$
$$\times \int d\Omega_{\hat{\mathbf{q}}_2} w(\hat{\mathbf{q}}_1) w(\hat{\mathbf{q}}_2) P_l(\hat{\mathbf{q}}_1 \cdot \hat{\mathbf{q}}_2) W_{l'}(\hat{\mathbf{q}}_1, \hat{\mathbf{q}}_2). \tag{26}$$

Using the expression for the window function for a noncircular beam in Eq. (15) the bias matrix can be written as

$$A_{ll'} = \frac{B_{l'}^2}{4\pi} \frac{(2l'+1)}{(2l+1)} \frac{l(l+1)}{l'(l'+1)} \times \sum_{n=-l}^{l} \sum_{m=-l'}^{l'} \left| \sum_{m'=-l'}^{l'} \beta_{l'm'} \right.$$
$$\times \left. \int d\Omega_{\hat{\mathbf{q}}} Y_{ln}^*(\hat{\mathbf{q}}) D_{mm'}^{l'}[\hat{\mathbf{q}}, \rho(\hat{\mathbf{q}})] w(\hat{\mathbf{q}}) \right|^2. \tag{27}$$

The above expressions in Eq. (26) and (27) are valid for a completely general noncircular beam with an arbitrary orientation at each point. The scan-pattern of the CMB experiment and relative orientation of the beam along it is encoded in the function $\rho(\hat{\mathbf{q}})$. The weight $w(\hat{\mathbf{q}})$ can account for nonuniform sky coverage. Analytical progress can be made when $w(\hat{\mathbf{q}}) \equiv w(\theta)$ and $\rho(\hat{\mathbf{q}}) = \rho(\theta)$ are fixed along a given declination, but we do not discuss further it here. When the beam transform, weight function and the scan-pattern are specified, the bias matrix can be evaluated numerically using Eq. (27). However, for mild deviations from circularity, the above expression also points to a perturbation expansion in the small beam distortion parameters, β_{lm}.

For obtaining fully analytical results, we set the weight function $w(\hat{\mathbf{q}}) = 1$, corresponding to a full, uniform sky coverage and also limit attention to scans with "nonrotating" beams where $\rho(\hat{\mathbf{q}}) = 0$. This is presented in the next subsections.

A. Circular symmetric beam

We first consider Eq. (27) for the simpler and well studied case of a circular beam. For clarity of presentation, we limit our discussion to full, uniform sky coverage ($w(\hat{\mathbf{q}}) = 1$). Results for nonuniform coverage with a circular beam are available in the literature [4,23,37].

Using the expression for the window function for circular beam Eq. (11) into the expression for the bias in Eq. (26) we recover

$$A_{ll'} = B_l^2 \delta_{ll'} \Rightarrow \langle \widetilde{C}_l \rangle = B_l^2 C_l. \tag{28}$$

For a full sky measurement with a circular beam, the bias matrix is diagonal, implying that there is no mixing of power between different multipoles. The true expectation value of the power spectrum can be obtained by dividing the pseudo-C_l estimator by the isotropic beam transform B_l^2.

Next we account for the noise contribution and recover the well-known result for a full sky observation. The pixel noise $n(\hat{\mathbf{q}})$ adds to the observed temperature, so that the resultant observed temperature

$$\widetilde{\Delta T}'(\hat{\mathbf{q}}) = \widetilde{\Delta T}(\hat{\mathbf{q}}) + n(\hat{\mathbf{q}}) \tag{29}$$

and we can readily obtain

$$\langle \widetilde{C}_l' \rangle = \langle \widetilde{C}_l \rangle + C_l^N = B_l^2 C_l + C_l^N, \tag{30}$$

where C_l^N is the angular power spectrum of the noise $n(\hat{\mathbf{q}})$ is a well determined quantity. The unbiased estimator for C_l obtained is

$$\widetilde{C}_l^{UB} = B_l^{-2}(\widetilde{C}_l' - C_l^N). \tag{31}$$

B. Noncircular beam

We obtain analytic results for the bias matrix for a full sky observation ($w(\hat{\mathbf{q}}) = 1$) with a noncircular beam that "does not rotate". The phrase "nonrotating" means that the orientation of the noncircular beam does not rotate about its axis (the pointing direction) while the pointing direction scans the sky implying that

$$\rho(\hat{\mathbf{q}}) = 0. \tag{32}$$

For nonrotating beam, the calculation of the bias is completely analytically tractable. The integral in the expression for the bias in Eq. (27) is given by

$$\int Y_{ln}^*(\hat{\mathbf{q}}) D_{mm'}^{l'}(\hat{\mathbf{q}}, 0) d\Omega_{\hat{\mathbf{q}}} = \sqrt{(2l+1)\pi} I_{mm'}^{ll'} \delta_{mn}, \tag{33}$$

where

$$I_{mm'}^{ll'} \equiv \int_{-1}^{1} d_{m0}^l(\theta) d_{mm'}^{l'}(\theta) d\cos\theta, \tag{34}$$

and $d_{mm'}^l(\theta)$ are Wigner-d functions related to Wigner-D functions

$$D_{mm'}^l(\hat{\mathbf{q}}, \rho) = e^{-im\phi} d_{mm'}^l(\theta) e^{-im'\rho}. \tag{35}$$

The analytic simplicity arises from the fact that for

$\rho(\hat{\mathbf{q}}) = 0$, the Wigner-$D$ function reduces to spherical harmonic function

$$Y_{lm}(\hat{\mathbf{q}}) = \sqrt{\frac{2l+1}{4\pi}} D_{m0}^l(\hat{\mathbf{q}}, 0). \tag{36}$$

In deriving the above equations we have used the orthogonality of the phases $\int_0^{2\pi} e^{-i(m-n)\phi} d\phi = 2\pi \delta_{mn}$.

Substituting the expression for the integral Eq. (33) into the expression for the bias in Eq. (27), we obtain

$$A_{ll'} = B_{l'}^2 \left(\frac{2l'+1}{4}\right) \frac{l(l+1)}{l'(l'+1)} \sum_{m=-L}^{L} \left| \sum_{m'=-l'}^{l'} \beta_{l'm'} I_{mm'}^{ll'} \right|^2, \tag{37}$$

where $L \equiv \min\{l, l'\}$ is the smaller between l and l'.

Further analytical progress is possible for smooth beam with mild deviations from circular symmetry through a perturbation in terms of the small beam distortion parameters, β_{lm}. We calculate the exact analytic expression for the leading order effect. Assuming a beam with reflection symmetry where β_{lm} are zero for odd m, the leading order effect comes at the second order, namely, $\beta_{l2}\beta_{l0}$ (see Eq. (18)). Neglecting, β_{lm} for $|m| > 2$, we obtain

$$A_{ll'} = B_{l'}^2 \left(\frac{2l'+1}{4}\right) \frac{l(l+1)}{l'(l'+1)}$$
$$\times \sum_{m=-L}^{L} [I_{m0}^{ll'} + \beta_{l'2}(I_{m2}^{ll'} + I_{m-2}^{ll'})]^2. \tag{38}$$

Next we obtain analytical expression for the two integrals, $I_{m0}^{ll'}$ and $I_{m2}^{ll'} + I_{m-2}^{ll'}$. The first one can be found in standard texts (e.g. [45]) given as

$$I_{m0}^{ll'} \equiv \int_{-1}^{1} d_{m0}^l(\theta) d_{m0}^{l'}(\theta) d\cos\theta = \frac{2}{2l+1} \delta_{ll'}. \tag{39}$$

For $m = 0$, writing $d_{00}^l(\theta)$ and $d_{02}^l(\theta)$ in terms of $P_l(\cos\theta)$ and its first derivative $P_l'(\cos\theta)$ we have shown in Appendix B that for odd values of $l + l'$, $I_{02}^{ll'} + I_{0-2}^{ll'} = 0$. For even values of $l + l'$,

$$I_{02}^{ll'} + I_{0-2}^{ll'} = \begin{cases} 8/\kappa & \text{if} \quad l < l' \\ 0 & \text{if} \quad l > l', \\ -(4l/\kappa)(l-1)/(2l+1) & \text{if} \quad l = l' \end{cases} \tag{40}$$

where $\kappa \equiv \sqrt{(l'-1)l'(l'+1)(l'+2)}$.

To evaluate $I_{m2}^{ll'} + I_{m-2}^{ll'}$ for nonzero m we expand $d_{m\pm2}l'(\theta)$ in terms of $d_{m0}^{l''}(\theta)$ using a recurrence relation of the Wigner-D functions (where l'' takes integer values between $l' - 2$ to $l' + 2$). The details are given in Appendix B. We obtain that $I_{m2}^{ll'} + I_{m-2}^{ll'} = 0$ for odd $l + l'$.

For even values of $l + l'$, if $L \equiv \min\{l, l'\} \geq |m| > 0$,

$$
I_{m2}^{ll'} + I_{m-2}^{ll'}
$$
$$
= \begin{cases} (4/\kappa)(|m| + 1)\sqrt{\frac{(l+|m|)!(l'-|m|)!}{(l-|m|)!-(l'+|m|)!}} & \text{if} \quad l < l' \\ (4/\kappa)(|m| - 1)\sqrt{\frac{(l-|m|)!(l'+|m|)!}{(l+|m|)!-(l'-|m|)!}} & \text{if} \quad l > l' \\ (4/\kappa)[|m| - (l^2 + l + 1)/(2l + 1)] & \text{if} \quad l = l'. \end{cases}
$$

$$(41)$$

The bias matrix including the leading order beam distortion (for nonrotating, reflection symmetric beams) can be summarized as

* For odd values of $l + l'$,

$$A_{ll'} = 0. \tag{42}$$

* For even values of $l + l'$,

$$
A_{ll'} = \begin{cases} (B_{l'}\beta_{l'2})^2\left(\frac{8l(l+1)(2l'+1)}{l'^2(l'+1)^2(l'-1)(l'+2)}\right)\left[2 + \sum_{m=1}^{l}\frac{(l-m)!(l'+m)!}{(l+m)!(l'-m)!}(m+1)^2\right] & \text{if} \quad l < l' \\ (B_{l'}\beta_{l'2})^2\left(\frac{8l(l+1)(2l'+1)}{l'^2(l'+1)^2(l'-1)(l'+2)}\right)\left[\sum_{m=1}^{l'}\frac{(l-m)!(l'+m)!}{(l+m)!(l'-m)!}(m-1)^2\right] & \text{if} \quad l > l' \\ \frac{B_l^2}{2l+1}\left[\left\{1 - 2\beta_{l2}\sqrt{\frac{l(l-1)}{(l+1)(l+2)}}\right\}^2 + 2\sum_{m=1}^{l}\left\{1 - 2\beta_{l2}\frac{(l^2+l+1)-(2l+1)m}{\sqrt{(l-1)l(l+1)(l+2)}}\right\}^2\right] & \text{if} \quad l = l' \end{cases}
$$

$$(43)$$

The nonzero off-diagonal terms in the bias matrix $A_{ll'}$ imply that the noncircular beam mixes the contribution of different multipoles from the actual power spectrum in the observed power spectrum. Off-diagonal elements in $A_{ll'}$ that arise from nonuniform/incomplete sky coverage have been studied earlier and are routinely accounted for in CMB experiments. Noncircular beam is yet another source of off-diagonal terms in the bias matrix and should be similarly taken into account. In general, CMB experiments have both noncircular beams and nonuniform/incomplete sky coverage that could lead to interesting features in $A_{ll'}$.

Although the analytical result is limited to mildly noncircular and nonrotating beam functions, it does bring to light certain generic features of the effect of noncircular beam functions. To be specific, we compute the elements $A_{ll'}$ for nonrotating *elliptic Gaussian* beams (see appendix A). The noncircularity of these beams is characterized by their eccentricity $e = \sqrt{1 - \sigma_2^2/\sigma_1^2}$, where σ_1 and σ_2 are the 1σ beamwidths along major and minor axes of the beam (see Table I). Many experiments have characterized their beams in terms of an elliptic Gaussian fit (e.g., [39,42,43]). A convenient advantage of elliptical beams is that the beam transform b_{lm} (and obviously, the beam distortion parameters, β_{lm}) can be expressed in a closed analytical form. The results expressed in terms of $l\bar{\sigma}$ are broadly independent of the average beam-size [41].

Figure 3 shows a density plot of the normalized bias matrix $A_{ll'}/(B_l B_{l'})$ for a nonrotating elliptical beam. The plot illustrates the importance of off-diagonal terms that arise due to the noncircular beam relative to the diagonal terms. The absence of coupling between multipoles separated by odd integers is evident. Also evident is the falloff as one moves away from the diagonal. The left panel of Fig. 4 shows that the off-diagonal elements of $A_{ll'}$ are important at $l\bar{\sigma} \sim 1$. The results are qualitatively independent of the average beam size $\bar{\sigma}$. The right panel Fig. 4 shows the strong dependence of the dominant off-diagonal element A_{ll+2} on the eccentricity of the beam.

The analytical results and numerical computations using Eq. (26) were compared. The numerical and analytical results match perfectly as shown in Fig. 4. Numerical computation involves the pixelized sky and the algorithm must ensure that this does not introduce spurious effects. We verify that $A_{ll'}$ has numerically negligible off-diagonal elements when the beam is circularly symmetric. The numerical computation for noncircular beam are verified to be robust to the pixelization of the sky.
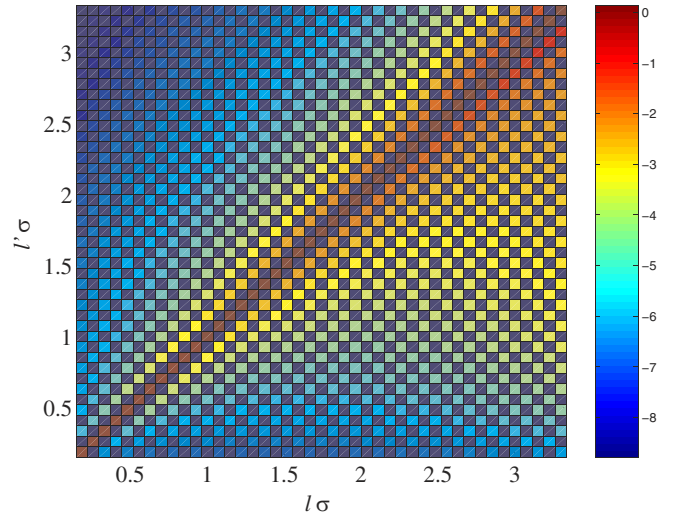

FIG. 3 (color online). The log of normalized bias matrix $A_{ll'}/(B_l B_{l'})$ is plotted for an elliptical beam of eccentricity $e = 0.6$ and mean beamwidth $\bar{\sigma} = 0.074$. The normalization is carried out so that the effect of noncircularity on the bias matrix can be easily compared to that for circular beams. Beam-rotation and cut-sky effects have not been considered in this figure. One notices that the off-diagonal elements of the bias matrix take significant values for $l\bar{\sigma} \gtrsim 1$.
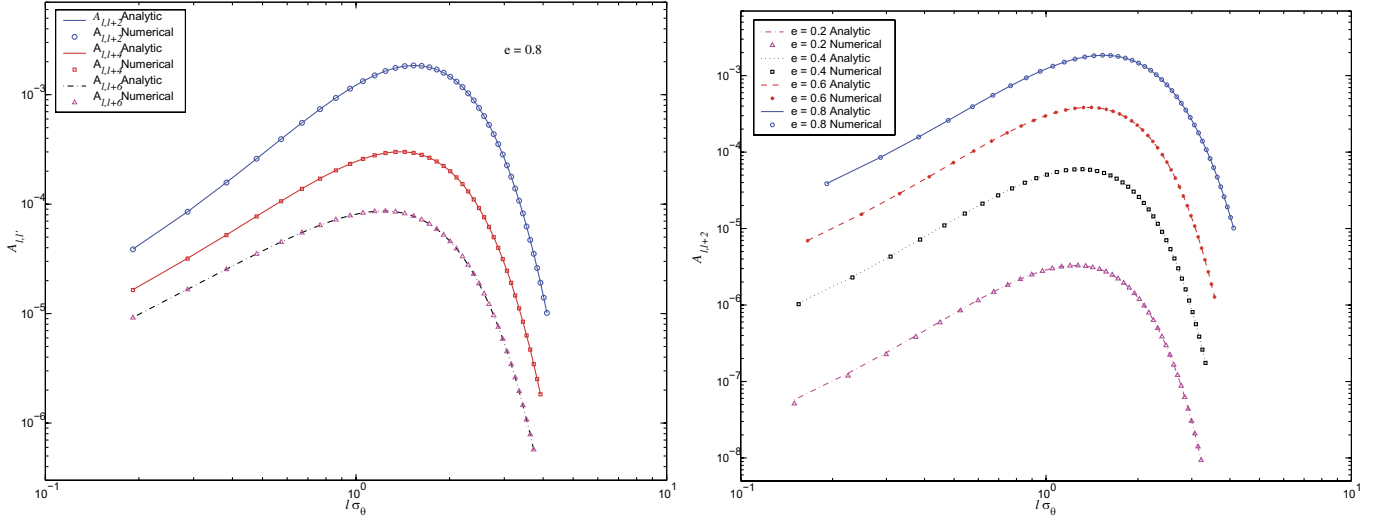
FIG. 4 (color online). Elements of the bias matrix $A_{ll'}$ are plotted in this figure as a function of multipole (l). The bias matrix relates the observed C_ls to their true values. When noncircular beams are used in CMB experiments, the bias matrix can be shown to be nondiagonal, thus implying mixing of power between multipoles. On the top panel, we plot $A_{ll'}$ for $l' - l = 2, 4, 6$. It is evident that the effect decreases as we move away from the diagonal and that it kicks in at $l\bar{\sigma} \sim 1$, for a beam of eccentricity $e = 0.8$. For the figure in the bottom panel, we plot A_{ll+2} for several beams of the same size but different eccentricities. Clearly, the effect also depends strongly on the noncircularity of the beam.

Next we illustrate effect of beam rotation and nonuniform sky coverage for a *hypothetical* experiment where $A_{ll'}$ have been computed numerically. The left panel of Fig. 5 shows (in log scale) the normalized bias matrix arising from a 2.5° circular beam including a nontrivial

$w(\hat{\mathbf{q}})$ in the form of a smoothed version of the galactic mask Kp2 of WMAP [26,46]. The right panel of the figure shows the *extra* effect that a rotating noncircular beam would introduce. We assume a simple "toy" beam-rotation along an equal declination scan strategy, where
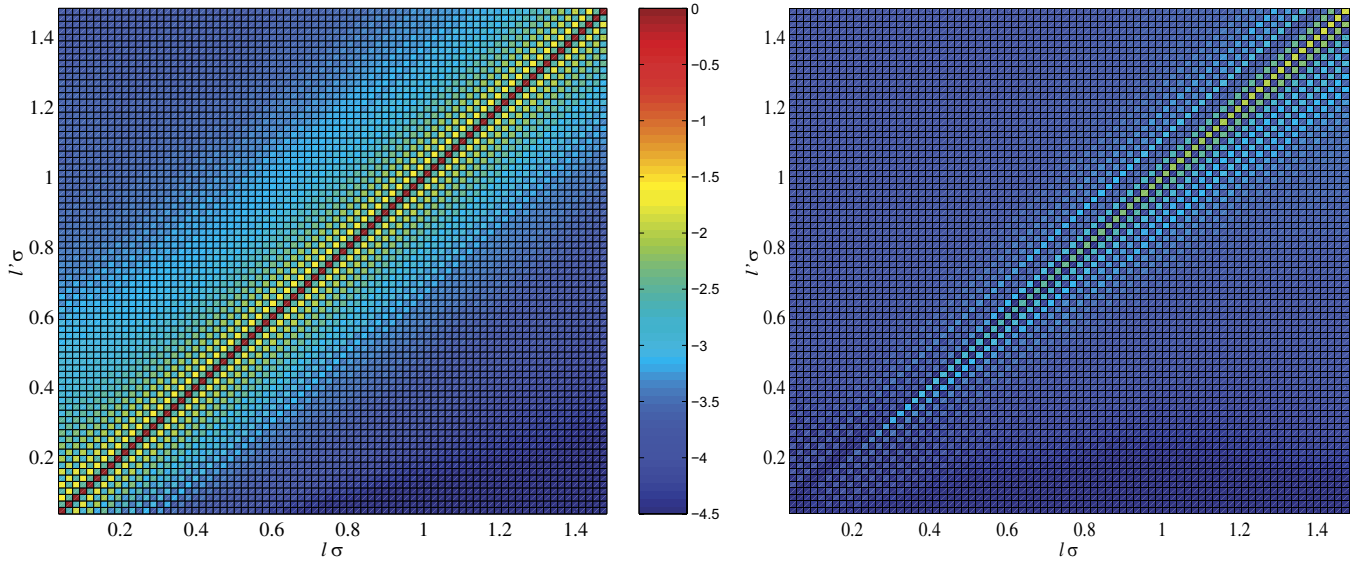

FIG. 5 (color online). The normalized bias matrix elements (on log scale, $\log[A_{ll'}/(B_l B_{l'})]$) of a hypothetical experiment with a scan-pattern (Eq. (44)) corresponding to a rotating, noncircular beam ($e = 0.6$) and nonuniform sky coverage are studied. The left panel shows the effect of nonuniform coverage alone (circular beam approximation). The right panel isolates the additional effect that arises due to the noncircularity of the beam and its rotation. We note that significant off-diagonal elements arise at $l\bar{\sigma} \geq 1$ from the noncircular beam comparable to that from the nonuniform coverage. The nonuniform coverage corresponds to a smoothed WMAP Kp2 galactic mask (smoothed from resolution of $N_{\text{side}} = 512$ to 64). We use a sufficiently high resolution beam with $\bar{\sigma} = 0.018$ ($\theta_{1/2} = 2.5°$) to ensure that the effects due to the galactic mask and the noncircular beam appear in distinct regions of the multipole space.

the beam continuously "rotates" by 2π for every complete pass at a given declination which implies the simple form

$$\rho(\hat{\mathbf{q}}) \equiv \rho(\theta, \phi) = \phi. \tag{44}$$

The elements here have been computed numerically using Eq. (26) retaining the leading order terms in the perturbation expansion of W_l in Eq. (18). The off-diagonal effects at low l are dominated by the cut-sky effect. The off-diagonal element $l\bar{\sigma} > \sim 1$ arise solely due to noncircular beam. The numerical computation illustrates the potentially large corrections that can arise due to noncircular beam that "rotate" on the sky. The numerical computations in this work pave the way for introducing realistic scan-pattern, beam-rotation and nonuniform sky coverage in a future extension to our work.

We summarize the following features of the bias matrix:

(1) There is no coupling between $\langle \widetilde{C}_l \rangle$ and $C_{l'}$ for odd values of $l + l'$,
(2) Coupling decreases as $|l - l'|$ increases,
(3) Coupling increases with eccentricity for fixed beam-size, and
(4) Size of the beam determines the multipole l value for which coupling will be maximum ($l\bar{\sigma} \sim 1$).

Figure 6 roughly indicates the level and nature of the effect of neglecting the noncircularity of the beam on CMB power estimation (for the conservative case of non-rotating beams). Consider the power spectrum $\widetilde{C}_l = \sum_{l'} A_{ll'} C_{l'}$ measured using a noncircular, elliptical Gaussian beam of a given eccentricity, e and average beamwidth, $\bar{\sigma}$. We compare the power spectrum obtained by deconvolving $\widetilde{C}_l$ with a circular, Gaussian beam of the beamwidth, $\bar{\sigma}$ with the true C_l. The lower panel shows that the error can be significant for multipole values beyond the inverse beamwidth even for modestly noncircular comparable to the WMAP beam maps (Q-band) discussed in the Appendix A.

Finally, we construct the unbiased estimator for the angular power spectrum. Invoking steps similar to the case of circular beams to account for the instrumental noise, we obtain

$$\langle \widetilde{C}'_l \rangle = \langle \widetilde{C}_l \rangle + C_l^N = \sum_{l'} A_{ll'} C_{l'} + C_l^N. \tag{45}$$

The unbiased estimator for the angular power spectrum is

$$\widetilde{C}_l^{UB} = \sum_{l'} A_{ll'}^{-1} (\widetilde{C}'_{l'} - C_{l'}^N). \tag{46}$$

IV. ERROR-COVARIANCE MATRIX

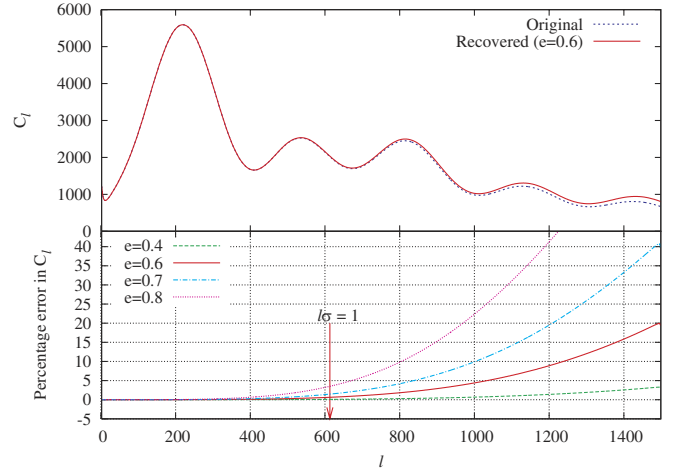The statistical error-covariance of the estimated angular power spectrum is defined as

FIG. 6 (color online). The effect of noncircular beam is studied for CMB power spectrum estimation by a CMB experiment with a WMAP-like noncircular beam. For illustration, we consider the best-fit (Power law) model to be the (fiducial) true C_l of the Universe shown as the solid line in the upper panel. Let $\widetilde{C}_l$ be the power spectrum measured by using a elliptical, Gaussian beam with eccentricity, $e = 0.6$, and $\bar{\sigma} = 0.0016$. The dashed line shows the $\widetilde{C}_l$ that would be inferred by deconvolving $\widetilde{C}_l$ with a circular beam assumption with beamwidth, $\bar{\sigma}$. The lower panel plots the relative error in the power spectrum recovered with a circular beam assumption for a measurements made with a noncircular beam with $e = 0.4$ to 0.8.

$$\mathrm{Cov}(\widetilde{C}_l, \widetilde{C}_{l'}) \equiv \langle (\widetilde{C}_l - \langle \widetilde{C}_l \rangle)(\widetilde{C}_{l'} - \langle \widetilde{C}_{l'} \rangle) \rangle. \tag{47}$$

In an idealized, noise free, CMB experiment with infinite angular resolution uniformly covering the full sky

$$\widetilde{C}_l = \frac{l(l+1)}{8\pi^2} \int d\Omega_{\hat{\mathbf{q}}_1} \int d\Omega_{\hat{\mathbf{q}}_2} \Delta T(\hat{\mathbf{q}}_1) \Delta T(\hat{\mathbf{q}}_2) P_l(\hat{\mathbf{q}}_1 \cdot \hat{\mathbf{q}}_2). \tag{48}$$

Using the property of Gaussian random fields that,

$$\langle \Delta T(\hat{\mathbf{q}}_1) \Delta T(\hat{\mathbf{q}}_2) \Delta T(\hat{\mathbf{q}}'_1) \Delta T(\hat{\mathbf{q}}'_2) \rangle$$
$$= \langle \Delta T(\hat{\mathbf{q}}_1) \Delta T(\hat{\mathbf{q}}_2) \rangle \langle \Delta T(\hat{\mathbf{q}}'_1) \Delta T(\hat{\mathbf{q}}'_2) \rangle$$
$$+ \langle \Delta T(\hat{\mathbf{q}}_1) \Delta T(\hat{\mathbf{q}}'_1) \rangle \langle \Delta T(\hat{\mathbf{q}}_2) \Delta T(\hat{\mathbf{q}}'_2) \rangle$$
$$+ \langle \Delta T(\hat{\mathbf{q}}_1) \Delta T(\hat{\mathbf{q}}'_2) \rangle \langle \Delta T(\hat{\mathbf{q}}'_1) \Delta T(\hat{\mathbf{q}}_2) \rangle \tag{49}$$

and Eq. (6), we recover the well-known result for full sky CMB maps

$$\mathrm{Cov}(\widetilde{C}_l, \widetilde{C}_{l'}) = \frac{2}{2l+1} \langle C_l \rangle^2 \delta_{ll'} = \frac{2}{2l+1} C_l^2 \delta_{ll'}, \tag{50}$$

corresponding to C_l being a sum of the squares of $2l + 1$ Gaussian variates, i.e. χ^2_{2l+1} distribution. The measured power spectrum at each multipole is independent (for full sky CMB maps). The variance of the power spectrum estimator is not zero even in the ideal case. Consequently, the measurement angular power spectrum from the one

available CMB sky map is inherently limited by an inevitable error the *Cosmic Variance*[4].

A. Circular beam

For measurements made with a circular beam, the temperature is a linear transform of the actual temperature (see Eq. (7)). So, it also represents a Gaussian random field. Hence, Eq. (49) remains valid even for observed temperature fluctuations. Moreover, the window function takes a simple form given in Eq. (11). Consequently, Eq. (6) gets modified to

$$\langle \widetilde{\Delta T}(\hat{\mathbf{q}}_1)\widetilde{\Delta T}(\hat{\mathbf{q}}_2)\rangle = \sum_{l=0}^{\infty} \frac{2l+1}{2l(l+1)} B_l^2 C_l P_l(\hat{\mathbf{q}}_1 \cdot \hat{\mathbf{q}}_2). \quad (51)$$

The covariance matrix

$$\mathrm{Cov}(\tilde{C}_l, \tilde{C}_{l'}) = \frac{2}{2l+1}\langle \tilde{C}_l\rangle^2 \delta_{ll'} = \frac{2}{2l+1}(B_l^2 C_l)^2 \delta_{ll'}, \quad (52)$$

remains diagonal for circular beams, i.e., the measured power spectrum at each multipole is independent of the power measured in the other multipoles. The second equality follows from Eq. (28).

Including the instrumental noise spectrum in the measured power spectrum C_l^N, we obtain

$$\mathrm{Cov}(\tilde{C}_l', \tilde{C}_{l'}') = \frac{2\delta_{ll'}}{2l+1}(\langle \tilde{C}_l\rangle + C_l^N)^2, \quad (53)$$

where we assume that the noise spectrum C_l^N is known much better and, in particular, does not suffer from cosmic variance. For the unbiased estimator given by Eq. (31), the well-known covariance matrix

$$\begin{aligned}\mathrm{Cov}(\tilde{C}_l^{UB}, \tilde{C}_{l'}^{UB}) &= B_l^{-4}\mathrm{Cov}(\tilde{C}_l', \tilde{C}_{l'}')\\ &= \frac{2\delta_{ll'}}{2l+1}(C_l + B_l^{-2}C_l^N)^2 \end{aligned} \quad (54)$$

is readily obtained from the linear transformation between C_l' and C_l^{UB} [47,48].

B. Noncircular beam

As expected, the covariance for the noncircular beam is considerably more complicated. We start with the general form of the two-point correlation function. Using Eq. (24), the general form of the covariance matrix is

$$\begin{aligned}\mathrm{Cov}(\tilde{C}_l, \tilde{C}_{l'}) &= \frac{ll'(l+1)(l'+1)}{(4\pi)^4}\\ &\times \sum_{l_1,l_2=0}^{\infty} \frac{(2l_1+1)(2l_2+1)}{l_1 l_2(l_1+1)(l_2+1)}C_{l_1}C_{l_2}\\ &\times \int d^4\Omega\, w(\hat{\mathbf{q}}_1)w(\hat{\mathbf{q}}_2)w(\hat{\mathbf{q}}'_1)w(\hat{\mathbf{q}}'_2)\\ &\times P_l(\hat{\mathbf{q}}_1 \cdot \hat{\mathbf{q}}_2)P_{l'}(\hat{\mathbf{q}}'_1 \cdot \hat{\mathbf{q}}'_2)[W_{l_1}(\hat{\mathbf{q}}_1, \hat{\mathbf{q}}'_1)\\ &\times W_{l_2}(\hat{\mathbf{q}}_2, \hat{\mathbf{q}}'_2) + W_{l_1}(\hat{\mathbf{q}}_1, \hat{\mathbf{q}}'_2)W_{l_2}(\hat{\mathbf{q}}_2, \hat{\mathbf{q}}'_1)],\end{aligned} \quad (55)$$

where for brevity we denote $d^4\Omega \equiv d\Omega_{\hat{\mathbf{q}}_1}d\Omega_{\hat{\mathbf{q}}_2}d\Omega_{\hat{\mathbf{q}}'_1}d\Omega_{\hat{\mathbf{q}}'_2}$.

Noting the interchangeability of the dummy variables $\hat{\mathbf{q}}'_1$ and $\hat{\mathbf{q}}'_2$, we combine the two terms in the above equation to obtain

$$\begin{aligned}\mathrm{Cov}(\tilde{C}_l, \tilde{C}_{l'}) &= 2\Bigg[\frac{ll'(l+1)(l'+1)}{(4\pi)^4}\Bigg]\\ &\times \sum_{l_1,l_2=0}^{\infty} \frac{(2l_1+1)(2l_2+1)}{l_1 l_2(l_1+1)(l_2+1)}C_{l_1}C_{l_2}\\ &\times \int d^4\Omega\, w(\hat{\mathbf{q}}_1)w(\hat{\mathbf{q}}_2)w(\hat{\mathbf{q}}'_1)w(\hat{\mathbf{q}}'_2)\\ &\times P_l(\hat{\mathbf{q}}_1 \cdot \hat{\mathbf{q}}_2)P_{l'}(\hat{\mathbf{q}}'_1 \cdot \hat{\mathbf{q}}'_2)W_{l_1}(\hat{\mathbf{q}}_1, \hat{\mathbf{q}}'_1)\\ &\times W_{l_2}(\hat{\mathbf{q}}_2, \hat{\mathbf{q}}'_2).\end{aligned} \quad (56)$$

We expand the Legendre Polynomials in terms of spherical harmonics (Eq. (5)) and use the expression for the window function in Eq. (15) to obtain

$$\begin{aligned}\mathrm{Cov}(\tilde{C}_l, \tilde{C}_{l'}) &= \frac{ll'(l+1)(l'+1)}{8\pi^2(2l+1)(2l'+1)}\\ &\times \sum_{l_1,l_2=0}^{\infty} \frac{(2l_1+1)(2l_2+1)}{l_1 l_2(l_1+1)(l_2+1)}C_{l_1}C_{l_2}B_{l_1}^2 B_{l_2}^2 \sum_{m=-l}^{l}\sum_{m'=-l'}^{l'}\sum_{m_1=-l_1}^{l_1}\sum_{m_2=-l_2}^{l_2}\Bigg\{\sum_{m_1',m_1''=-l_1}^{l_1}\beta_{l_1 m_1'}\beta_{l_1 m_1''}^* \int d\Omega_{\hat{\mathbf{q}}_1}w(\hat{\mathbf{q}}_1)Y_{lm}^*(\hat{\mathbf{q}}_1)\\ &\times D_{m_1 m_1'}^{l_1}[\hat{\mathbf{q}}_1, \rho(\hat{\mathbf{q}}_1)]\int d\Omega_{\hat{\mathbf{q}}'_1}w(\hat{\mathbf{q}}'_1)Y_{l'm'}(\hat{\mathbf{q}}'_1)D_{m_1 m_1''}^{l_1*}[\hat{\mathbf{q}}'_1, \rho(\hat{\mathbf{q}}'_1)] \sum_{m_2',m_2''=-l_2}^{l_2}\beta_{l_2 m_2'}^*\beta_{l_2 m_2''}\\ &\times \int d\Omega_{\hat{\mathbf{q}}_2}w(\hat{\mathbf{q}}_2)Y_{lm}(\hat{\mathbf{q}}_2)D_{m_2 m_2'}^{l_2*}[\hat{\mathbf{q}}_2, \rho(\hat{\mathbf{q}}_2)]\int d\Omega_{\hat{\mathbf{q}}'_2}w(\hat{\mathbf{q}}'_2)Y_{l'm'}^*(\hat{\mathbf{q}}'_2)D_{m_2 m_2''}^{l_2}[\hat{\mathbf{q}}'_2, \rho(\hat{\mathbf{q}}'_2)]\Bigg\},\end{aligned} \quad (57)$$

---

[4]This is a direct consequence of the sphere being compact and, consequently, an inevitable, rigid lower bound on the uncertainty in the measurement of angular power spectrum at a given multipole l. Otherwise, the effect is the similar to the well-known sample variance of a finite data-stream

as the general expression for error-covariance for angular power spectrum for noncircular beams. Note that even for full, uniform sky observations, $w(\hat{\mathbf{q}}) = 1$, the error-covariance matrix is no longer diagonal.

To make further progress analytically, we restrict to the case of uniform, full sky coverage ($w(\hat{\mathbf{q}}) = 1$) with no beam-rotation ($\rho(\hat{\mathbf{q}}) = 0$). Using the integration of Eq. (33) and after a considerable algebra we may write the expression for covariance as

$$
\mathrm{Cov}(\tilde{C}_l, \tilde{C}_{l'}) = \frac{ll'(l+1)(l'+1)}{8}
$$
$$
\times \sum_{m=-L}^{L} \Bigg[\sum_{l_1=|m|}^{\infty} B_{l_1}^2 C_{l_1} \frac{(2l_1+1)}{l_1(l_1+1)}
$$
$$
\times \sum_{m_1'=-l_1}^{l_1} \beta_{l_1 m_1'} I_{mm_1'}^{ll_1} \sum_{m_1''=-l_1}^{l_1} \beta_{l_1 m_1''}^* I_{mm_1''}^{l'l_1} \Bigg]^2
$$
$$
\tag{58}
$$

where $L = \min\{l, l'\}$ is the smaller between l and l'. The integrals $I_{mm'}^{ll'}$ are defined in Sec. III and the analytical expressions for $m' = 0, \pm 2$ are given. It is straightforward to verify that the above equation correctly reproduces the expression for the error-covariance in the circular beam case given by Eq. (52).

For evaluation of the covariance matrix, we note that though the summation over l_1 runs from 0 to ∞, the contributions are significant only around $l \sim 1/\bar{\sigma}$ and the summation can be truncated suitably. Further, for most beams we can confine to the leading order approximation as in Eq. (18), by neglecting all the β_{lm}'s for $m \geq 4$. For mild deviations from circular beams, the observed power spectrum at different multipoles are weakly correlated ($\sim \beta_{l2}\beta_{l'2}$). The error-covariance matrix can be diagonalized to find the independent linear combinations of estimators (eigenvectors), and the variances of theses independent estimators are given by the corresponding eigenvalues. These eigenvalues are necessarily larger that the cosmic variance corresponding to a circular beam.

The inclusion of instrumental noise is similar to what was done in the circular beam case. The covariance

$$
\mathrm{Cov}(\tilde{C}_l', \tilde{C}_{l'}') = \mathrm{Cov}(\tilde{C}_l, \tilde{C}_{l'})
$$
$$
+ \frac{2\delta_{ll'}}{2l+1} [2\langle \tilde{C}_l \rangle C_l^N + (C_l^N)^2] \tag{59}
$$

clearly reproduces the result in Eq. (52) in the limit of a circular beam. Figure 7 shows a density plot of the elements of the covariance matrix for a noncircular (elliptical) beam with no rotation. In contrast to the case for incomplete (cut) sky case, where the effects are at small l (see [4]), the noncircular beam affects the large multipoles region ($l\bar{\sigma} \geq 1$). The pseudo-C_l approach is close to optimal for large l hence it may be more important to account for noncircular beams effects than the cut-sky,
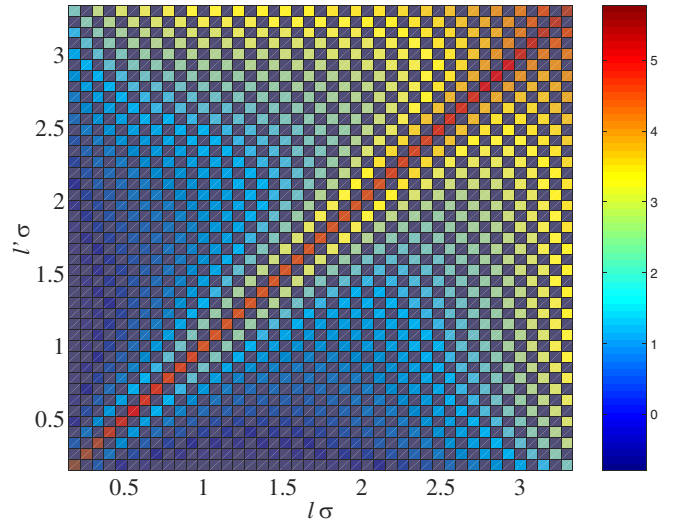

FIG. 7 (color online). Log of the normalized covariance matrix $\mathrm{Cov}(C_l, C_{l'})/(B_l B_{l'})^2$ (in the units of $(\mu K)^4$) is plotted for an elliptical beam of eccentricity $e = 0.6$ and mean beam-width $\bar{\sigma} = 0.074$. Because of the noncircularity of the beam, the error in CMB angular power spectrum estimate at different multipoles are no longer independent. We notice that the off-diagonal elements of the error-covariance matrix are pronounced for $l\bar{\sigma} \geq 1$.

since it is possible to use maximum likelihood estimator for small l.

The error-covariance matrix for the unbiased estimator Eq. (46) for noncircular beams is given by

$$
\mathrm{Cov}(\tilde{C}_l^{UB}, \tilde{C}_{l'}^{UB}) = \sum_{l_1} \sum_{l_2} A_{ll_1}^{-1} A_{l'l_2}^{-1} \mathrm{Cov}(\tilde{C}_{l_1}', \tilde{C}_{l_2}')
$$
$$
= \sum_{l_1} \sum_{l_2} \alpha_{ll_1} \alpha_{l'l_2} (B_{l_1} B_{l_2})^{-2}
$$
$$
\times \Bigg[\mathrm{Cov}(\tilde{C}_l, \tilde{C}_{l'}) + \frac{2\delta_{ll'}}{2l+1} \{2\langle \tilde{C}_l \rangle C_l^N
$$
$$
+ (C_l^N)^2 \} \Bigg], \tag{60}
$$

where the matrix $\alpha_{ll'} \equiv B_{l'}^{-2} A_{ll'}^{-1}$, being very close to identity, demonstrates that the beam-modified cosmic variance part of the covariance of unbiased estimator weakly depends on B_l's, whereas the noise part depends on them significantly.

V. DISCUSSION AND CONCLUSION

We present an analytic framework for addressing the effect of noncircular experimental beam function in the estimation of the angular power spectrum C_l of CMB anisotropy. Noncircular beam effects can be modeled into the covariance functions in approaches related to maximum likelihood estimation [9,10] and can also be included in the Harmonic ring [16] and ring-torus

estimators [17]. The latter is promising since it reduces the computational costs from N^3 to N^2. However, all these methods are computationally prohibitive for high resolution maps and, at present, the computationally economical approach of using a pseudo-C_l estimator appears to be a viable option for extracting the power spectrum at high multipoles [4]. The pseudo-C_l estimates have to be corrected for the systematic biases. While considerable attention has been devoted to the effects of incomplete/nonuniform sky coverage, no comprehensive or systematic approach is available for noncircular beam. The high sensitivity, full (large) sky observation from space (long duration balloon) missions have alleviated the effect of incomplete sky coverage and other systematic effects such as the one we consider here have gained more significance. Nonuniform coverage, in particular, the galactic masks affect only CMB power estimation at the low multipoles. Recently proposed hybrid scheme promotes a strategy where the power spectrum at low multipoles is estimated using optimal Maximum Likelihood methods and pseudo-C_l are used for large multipoles.

We have shown that noncircular beam is an effect that dominates at large l comparable to the inverse beam-width. For high resolution experiments, the optimal maximum likelihood methods which can account for noncircular beam functions are computationally prohibitive. In implementing pseudo-C_l estimation, the noncircular beam effect could dominate over the effects of more well-studied effect of nonuniform sky coverage. Our work provides a convenient approach for estimating the magnitude of this effect in terms of the leading order deviations from a circular beam. The perturbation approach is very efficient. For most CMB experiments the leading few orders capture most of the effect of beam noncircularity. The perturbation approach has allowed the development of computationally rapid method of computing window functions [41]. Our work may similarly yield computationally rapid methods correcting for beam noncircularity.

The quantitative estimates of the off-diagonal matrix elements of the bias and error-covariance for nonrotating beam graphically illustrate the general features that can be gleaned from our analytic results. They show that the beam noncircularity affects the C_l estimation on multipoles larger than the inverse beamwidth. A strong dependence on the eccentricity of the beam is also seen. *We caution against interpreting these results as a measure of the noncircular beam effects for any real CMB experiment.* The analytical results are limited to nonrotating beams and uniform sky coverage. Numerical results do not include scan-pattern of any known experiment. Numerical calculations of the bias matrix for a toy scanning strategy where the beam rotates on the sky indicates the possibility of significant corrections. The bias due to nonuniform sky coverage can have interesting coupling

to the bias from beam noncircularity. On the other hand, it has also been shown that effects of noncircular beams can be diluted if the scan-pattern is such that each point in the sky is revisited by the beam with a different orientation at different time [39]. The numerical implementation of our method can readily accommodate the case when pixels are revisited by the beam with different orientations. Evaluating the realistic bias and error-covariance for a specific CMB experiment with noncircular beams would require numerical evaluation of the general expressions for $A_{ll'}$ in Eqs. (27) using real scan strategy and account for inhomogeneous noise and sky coverage. We defer such an exercise to future work.

It is worthwhile to note in passing that the angular power C_l contains all the information of Gaussian CMB anisotropy only under the assumption of statistical isotropy. Gaussian CMB anisotropy map measured with a noncircular beam corresponds to an underlying correlation function that violates statistical isotropy. In this case, the extra information present may be measurable using, for example, the bipolar power spectrum [49]. Even when the beam is circular the scanning pattern itself is expected to cause a breakdown of statistical isotropy of the measured CMB anisotropy [37]. For a noncircular beam, this effect could be much more pronounced and, perhaps, presents an interesting avenue of future study.

In addition to temperature fluctuations, the CMB photons coming from different directions have a random, linear polarization. The polarization of CMB can be decomposed into E part, with even parity and B part, with odd parity. Besides the angular spectrum C_l^{TT}, the CMB polarization provides three additional spectra, C_l^{TE}, C_l^{EE} and C_l^{BB} which are invariant under parity transformations. The level of polarization of the CMB being about a tenth of the temperature fluctuation, it is only very recently that the angular power spectrum of CMB polarization field has been detected. The Degree Angular Scale Interferometer has measured the CMB polarization spectrum over limited band of angular scales in late 2002 [50]. The WMAP mission has also detected CMB polarization [51]. WMAP is expected to release the CMB polarization maps very soon. Correcting for the systematic effects of a noncircular beam for the polarization spectra is expected to become important soon. Our work is based on the perturbation approach of [41] which has been already been extended to the case of CMB polarization [42]. Extending this work to the case CMB polarization is another line of activity we plan to undertake in the near future.

In summary, we have presented a perturbation framework to compute the effect of noncircular beam function on the estimation of power spectrum of CMB anisotropy. We not only present the most general expression including nonuniform sky coverage as well as a noncircular beam that can be numerically evaluated but also provide elegant

analytic results in interesting limits. In this work, we have skipped over the effect of noncircular beam functions on map-making step. In simple scanning strategies, our results may be readily applied in this context. As CMB experiments strive to measure the angular power spectrum with increasing accuracy and resolution, the work provides a stepping stone to address a rather complicated systematic effect of noncircular beam functions.

ACKNOWLEDGMENTS

APPENDIX A: ELLIPTICAL GAUSSIAN FIT TO THE WMAP BEAM MAPS

We briefly describe an exercise in characterizing noncircular beams in CMB experiments using the beam maps of the WMAP mission. We analyzed the WMAP raw beam images in the Q1, V1, and W1 [46,52] bands using two different standard software packages. We use the elliptical Gaussian fit allowed by the well-known radio-astronomy software, AIPS, and a more elaborate ellipse fitting routine available within the standard astronomical image/data processing software IRAF. The ELLIPSE task in the STSDAS package of IRAF, which uses the widely known ellipse fitting routines by Jedrzejewski [53], allows independent elliptical fits to the isophotes. This significant greater degree of freedom in fitting to the noncircular beam allows us to assess whether a simple elliptical Gaussian fit is sufficient. The three bands see Jupiter in the two horns (labeled A and B) as a point source. The fitting routine fits ellipses along isointensity contours of the beam image, parametrized by position angle (PA), ellipticity ($\bar{\epsilon}$) and position of the center. Each of these parameters can be independently varied. The distance between successive ellipses can also be independently varied. The eccentricity e is related to ellipticity $\bar{\epsilon}$ as $e = \sqrt{1 - (1 - \bar{\epsilon})^2}$ (Please see Table I).

We fit the beams in two different ways: (a) by holding the ellipticity constant to $\bar{\epsilon} = 0.05$ and freely varying the position angle and center and (b) fixing the center to be the pixel with the highest intensity (normalized to 1.0 at the central pixel) and varying ellipticity and position angle. In the first case, we get the closest approximation to circular beam profiles as used in WMAP data analysis.

TABLE II. The result of ellipse fitting using IRAF on the Q1, V1, and W1 beams of the WMAP experiments. The frequency quoted is the ''effective'' frequency of the corresponding band from Page et al. [52]. The presence of substructures in the W1 band makes it difficult to fit elliptical contours to the beam.

Beam	Frequency (GHz)	Eccentricity	Position Angle (degree)
Q1 (A)	40.9	0.65	+80
Q1 (B)	40.9	0.67	-80
V1 (A)	60.3	0.48	+60
V1 (B)	60.3	0.45	-60
W1 (A)	93.5	0.40	$\cdots$[a]

[a]Not well determined by the IRAF ellipse fitting routine.

This beam has no azimuthal (ϕ) dependence. In the latter case, we get the elliptical profile of the WMAP beam which depends on both the polar (θ) and azimuthal (ϕ) distance from the pointing direction. Notice that in this case it is sufficient to provide the intensity along a particular direction (usually, the semimajor axis or $\phi = 0$) and the ellipticity $\bar{\epsilon}$. The results are tabulated in Table II

Even a visual inspection reveals that the Q1 beam map plotted in Fig. 2 is noncircular and the isointensity contours distinctly elliptical. Thus it comes as no surprise that the error bars as shown in Fig. 8 for circularized beam are larger than those for the elliptical profile. As a consis-
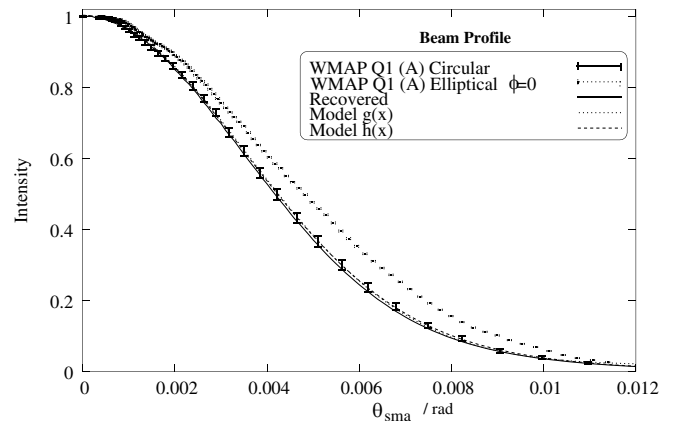

FIG. 8. The beam profile is characterized by intensity along the semimajor axis (SMA). The beam in Q-band for WMAP experiment was analyzed using IRAF and fitted to both circular and elliptical profiles. We have plotted the best-fit circular profile (solid error bars) and overlaid the profile recovered by inverting the WMAP beam transforms, available at LAMBDA website (solid line). Two analytical models for circular beam profile $g(\theta)$ and $h(\theta)$ are also considered, and the best-fit profiles are overlaid. We find that these models are consistent with the IRAF and WMAP data. We have also plotted the best-fit elliptical profile along SMA (broken error bar). Notice that the error bars in this case are much smaller than those for circular profile, implying a better agreement with the data.

tency check, we take the WMAP Q1 beam transfer function B_l from WMAP first year data archived at publicly available LAMBDA site [46] and "recover" the circular beam profile $B(\theta)$ using Eq. (10).

From Fig. 8, it is clear that this "recovered" beam profile is in good agreement with that obtained by IRAF. This allows us to make some statements about the profile fitting in CMB experiments, in the context of WMAP beams. The beam profile $B(\theta)$ has been modeled as a Gaussian times a sum of even order Hermite polynomials (H_{2n}) by the WMAP team [52]. To compare, we have also modeled the beam profile with a function $h(\theta)$ given by

$$h(\theta) = \exp\left(-\frac{1}{2}\alpha\theta^2\right)[h_0 + h_2 H_2(\theta) + h_4 H_4(\theta)], \quad (A1)$$

where α, h_0, h_2 and h_4 are unknown parameters to be fixed by least squared method. We found that this model fits the data very well with a reduced χ^2 of about 0.7. However, on closer analysis, it is found that the chief role of the Hermite polynomials is to add a constant baseline over and above the Gaussian. To test this hypothesis, we choose another form of the fitting function $g(\theta)$ given by

$$g(\theta) = g_0 + g_1 \exp\left(-\frac{1}{2}g_2\theta^2\right), \quad (A2)$$

where g_0, g_1 and g_2 are parameters of the model. It is very interesting to note that this model also fits the data very well with a reduced χ^2 of about 0.8 for the best fitted parameters. In all fairness, $g(\theta)$ serves as a simpler model for the beam profile. We cannot point to the precise origin for the baseline. However, such "skirts" in beam responses are not uncommon in radio-astronomy. At this point, our observation should perhaps merit a curious aside, if not as an alternative approach to beam modeling. Our best-fit models $g(\theta)$ and $h(\theta)$, along with the IRAF fitted data points to the WMAP Q1 (A) beam is shown in Fig. 8.

As shown earlier in this paper, the effects of noncircularity of the CMB experimental beams show up in the power-spectral density estimates through the off-diagonal elements of the bias matrix $A_{ll'}$. As shown in Eq. (27), these in turn can be expressed in terms of the leading components of the harmonic transform of the beam. In general the harmonic decomposition of a non-circular beam may have to be done numerically. But for the particular case of an elliptical Gaussian beam, a closed form expression given by Eq. (20) serves as a useful test bed for us. Thus another motivation for fitting ellipses to WMAP beams using IRAF was to get a handle on the eccentricity of these beams so as to find the harmonic transform components of an elliptical Gaussian beam of similar eccentricity. This allows us to give more realistic estimates of the effect of noncircularity of the beam on C_l estimates.
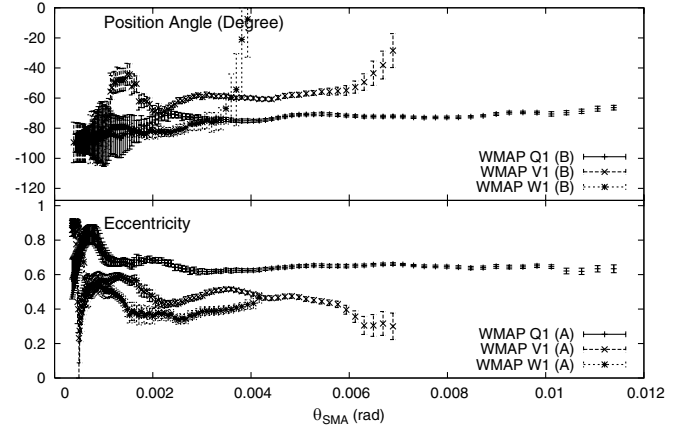

FIG. 9. The beams for WMAP experiment in three bands Q, V and W for both the horns (A and B) were fitted to elliptical profiles using IRAF. The plot above shows the fitted eccentricity and position angle along the semimajor axis (SMA). The presence of side-bands in the smaller beams (W band) makes it difficult for IRAF to model them sufficiently well. However, in the Q1 band, such substructures in the beam are not present thus allowing the IRAF ellipse fitting routine to fit reasonably good ellipses which have consistent eccentricities ($e \sim 0.65$) and position angles all along the SMA. The V1 beam is smaller in extent than the Q1 beam and its eccentricity was determined to be $e \sim 0.46$ using IRAF. The highest resolution beam in in W1 band, whose eccentricity was determined to be $e \sim 0.40$.

It is interesting to note how the fitted eccentricities vary as a function of the distance along the semimajor axis of the fitted ellipses for various beams. The smaller beams (V1 and W1) have sufficient substructure in the form of side-lobes which throws the ellipse fitting routine off course. However, where the substructure is less pronounced, we find that the eccentricities of the fitted ellipses takes a constant value. Toward the center of the ellipses, there are far too few pixels to average over, which in turn manifests as large error bars in the eccentricities and position angles of the ellipses. In Fig. 9, we notice that the Q1 beam has a very elliptical profile with eccentricity $e > \sim 0.65$ and position angle of about 75°. We also fitted the Q1 (A) beam to an elliptical Gaussian model using radio-astronomy standard data analysis software AIPS and got consistent numbers for the eccentricity. However the IRAF modeling gives us more freedom to vary the eccentricity and position angle as we move away from the center of the ellipse and the result is that the beam is modeled more accurately.

APPENDIX B: DETAILS OF ANALYTIC DERIVATIONS

In the appendix we provide the details of the analytical steps involved in deriving some of the expressions used in the main text. This is designed to keep the paper self-contained and easy to extend.

First, we outline the steps involved in evaluating the integral $I_{02}^{ll'} + I_{0-2}^{ll'} = 2\int_{-1}^{1} d_{00}^{l}(\theta)d_{02}^{l'}(\theta)d\cos\theta$ to obtain the result in Eq. (40).

Using the expressions [41,45] for d_{00}^{l} and d_{02}^{l} in terms of Legendre Polynomials and its derivatives,

$$\int_{-1}^{1} d_{00}^{l}(\theta)d_{02}^{l'}(\theta)d\cos\theta = -\frac{l'(l'+1)}{\kappa}\int_{-1}^{1} P_{l}(x)P_{l'}(x)dx + \frac{2}{\kappa}\int_{-1}^{1} xP_{l}(x)P'_{l'}(x)dx,$$
(B1)

where, $\kappa \equiv \sqrt{(l-1)l(l+1)(l+2)}$. The first integral is simply the orthogonality of Legendre polynomials

$$\int_{-1}^{1} P_{l}(x)P_{l'}(x)dx = \frac{2\delta_{ll'}}{2l+1}.$$
(B2)

Further, we can show that for odd values of $l + l'$,

$$\int_{-1}^{1} xP_{l}(x)P'_{l'}(x)dx = 0,$$
(B3)

and for even values of $l + l'$,

$$\int_{-1}^{1} xP_{l}(x)P'_{l'}(x)dx = \begin{cases} 2 & \text{if } l < l' \\ 0 & \text{if } l > l' \\ 2l/(2l+1) & \text{if } l = l' \end{cases}$$
(B4)

Assembling all these we can derive Eq. (40).

Next we evaluate the more general integral $I_{m2}^{ll'} + I_{m-2}^{ll'} \equiv \int_{-1}^{1} d_{m0}^{l}(\theta)[d_{m2}^{l'}(\theta) + d_{m-2}^{l'}(\theta)]d\cos\theta$ to obtain the expression in Eq. (41). The first step is to express $d_{m\pm2}^{l}(\theta)$ in terms of $d_{m0}^{l'}(\theta)$. Using the recurrence relations for Wigner D functions (see eq. (4) in Sec. 4.8.1, [45]) and using the fact that

$$D_{mm'}^{l}(\phi, \theta, \rho) = e^{-im\phi}d_{mm'}^{l}(\theta)e^{-im'\rho}$$
(B5)

we get the recurrence relations for Wigner-d functions:

$$\sin\theta d_{mm'+1}^{l}(\theta) = \frac{\sqrt{(l^2-m^2)(l+m')(l+m'+1)}}{l(2l+1)}d_{mm'}^{l-1}(\theta)$$
$$- \frac{m\sqrt{(l-m')(l+m'+1)}}{l(l+1)}d_{mm'}^{l}(\theta)$$
$$- \frac{\sqrt{[(l+1)^2-m^2](l-m')(l-m'+1)}}{(l+1)(2l+1)}$$
$$\times d_{mm'}^{l+1}(\theta).$$
(B6)

Using these relations for d_{m2}^{l} we may write,

$$d_{m2}^{l}(\theta) = \frac{\kappa}{\sin^2(\theta)}[\kappa_0 d_{m0}^{l}(\theta) + \kappa_1 d_{m0}^{l+1}(\theta) + \kappa_{-1}d_{m0}^{l-1}(\theta) + \kappa_2 d_{m0}^{l+2}(\theta) + \kappa_{-2}d_{m0}^{l-2}(\theta)],$$
(B7)

where

$$\kappa_0 \equiv \frac{m^2}{l^2(l+1)^2} - \frac{l^2-m^2}{l^2(4l^2-1)} - \frac{(l+1)^2-m^2}{(l+1)^2(2l+1)(2l+3)},$$

$$\kappa_1 \equiv 2m\frac{\sqrt{(l+1)^2-m^2}}{l(l+1)(l+2)(2l+1)},$$

$$\kappa_{-1} \equiv -2m\frac{\sqrt{l^2-m^2}}{l(l^2-1)(2l+1)},$$

$$\kappa_2 \equiv \frac{\sqrt{[(l+1)^2-m^2][(l+2)^2-m^2]}}{(l+1)(l+2)(2l+1)(2l+3)},$$

$$\kappa_{-2} \equiv \frac{\sqrt{(l^2-m^2)[(l-1)^2-m^2]}}{l(l-1)(4l^2-1)}.$$

Also, since $d_{m-2}^{l}(\theta) = (-1)^{l+m}d_{m2}^{l}(\pi-\theta)$ and $d_{m0}^{l}(\pi-\theta) = (-1)^{l+m}d_{m0}^{l}(\theta)$ we can write,

$$d_{m-2}^{l}(\theta) = \frac{\kappa}{\sin^2(\theta)}[\kappa_0 d_{m0}^{l}(\theta) - \kappa_1 d_{m0}^{l+1}(\theta) - \kappa_{-1}d_{m0}^{l-1}(\theta) + \kappa_2 d_{m0}^{l+2}(\theta) + \kappa_{-2}d_{m0}^{l-2}(\theta)].$$
(B8)

Using the expression for $d_{m\pm2}$ we can make the following substitution

$$d_{m2}^{l}(\theta) + d_{m-2}^{l}(\theta) = 2\kappa[\kappa_0 d_{m0}^{l}(\theta) + \kappa_2 d_{m0}^{l+2}(\theta) + \kappa_{-2}d_{m0}^{l-2}(\theta)]/\sin^2\theta,$$
(B9)

in the integral we seek to evaluate. We use the following integral for $l \le l'$ and $L = \min\{l, l'\} \ge |m| > 0$,

$$\int_{-1}^{1} d_{m0}^{l}(\theta)d_{m0}^{l'}(\theta)\frac{d\cos\theta}{\sin^2\theta}$$
$$= \begin{cases} \frac{1}{|m|}\sqrt{\frac{(l+|m|)!(l'-|m|)!}{(l-|m|)!(l'+|m|)!}} & \text{even } l+l' \\ 0 & \text{odd } l+l' \end{cases}$$
(B10)

and obviously, for $l > l'$, l and l' have to be interchanged in the above expression. We then obtain $I_{m2}^{ll'} + I_{m-2}^{ll'}$ as given in Eq. (41).

The integral in Eq. (B10) can also be readily derived. We use the fact that

$$d_{m0}^{l}(\theta) = (-1)^m\sqrt{\frac{(l-m)!}{(l+m)!}}P_{l}^{m}(\cos\theta),$$
(B11)

which leads to

$$\int_{-1}^{1} d_{m0}^{l}(\theta)d_{m0}^{l'}(\theta)\frac{d\cos\theta}{\sin^2\theta}$$
$$= \sqrt{\frac{(l-m)!(l'-m)!}{(l+m)!(l'+m)!}}\int_{-1}^{1} P_{l}^{m}(x)P_{l'}^{m}(x)\frac{dx}{1-x^2}.$$
(B12)

The symmetry of Associated Legendre Polynomials, $P_{l}^{m}(-x) = (-1)^{l+m}P_{l}^{m}(x)$ dictates that the integrand is antisymmetric for odd values of $l + l'$, hence the integral is zero. However for even values of $l + l'$, we can evaluate the integral in the following manner. One of the recurrence relations for Associated Legendre Polynomials is ([54], Sec. 12.5.)

$$P_l^m(x) = P_{l-2}^m(x) + (2l-1)\sqrt{1-x^2}P_{l-1}^{m-1}(x). \quad \text{(B13)}$$

Using Eq. (B13) we can write,

$$\int_{-1}^{1} P_l^m(x)P_{l'}^m(x)\frac{dx}{1-x^2} = \int_{-1}^{1} P_l^m(x)P_{l'-2}^m(x)\frac{dx}{1-x^2}$$
$$+(2l'-1)\int_{-1}^{1} P_l^m(x)P_{l'-1}^{m-1}(x)$$
$$\times \frac{dx}{\sqrt{1-x^2}}. \quad \text{(B14)}$$

We have provided a proof that the second integral on the right is zero at the end of this section. Thus, from Eq. (B14) we have

$$\int_{-1}^{1} P_l^m(x)P_{l'}^m(x)\frac{dx}{1-x^2} = \int_{-1}^{1} P_l^m(x)P_{l'-2}^m(x)\frac{dx}{1-x^2}. \quad \text{(B15)}$$

In this way we can keep reducing l' by two each time until it equals with l (since $l + l'$ is even and $l < l'$ it *will* reduce to l). Thus, we have shown that,

$$\int_{-1}^{1} P_l^m(x)P_{l'}^m(x)\frac{dx}{1-x^2} = \int_{-1}^{1} [P_l^m(x)]^2\frac{dx}{1-x^2}$$
$$= \frac{1}{m}\frac{(l+m)!}{(l-m)!}, \quad \text{(B16)}$$

where the second equality follows from the evaluation of a standard integral, which can be obtained, for example, from [54]. Substituting in Eq. (B12) we can evaluate the integral for $m > 0$. Clearly Eq. (B16) is valid for $l = l'$. For $l > l'$, l should be replaced by l' in that equation. Moreover, using the property $d_{-m0}^l(\theta) = (-1)^m d_{m0}^l(\theta)$, we can express the integral for any $m \neq 0$, as given in Eq. (B10).

Finally we prove the result used in simplifying Eq. (B14) that for even values of $l + l'$ and $l < l'$,

$$\int_{-1}^{1} P_l^m(x)P_{l'-1}^{m-1}(x)\frac{dx}{\sqrt{1-x^2}} = 0. \quad \text{(B17)}$$

Using the recurrence relation of Legendre Polynomials in Eq. (B13), we can write

$$\int_{-1}^{1} P_l^m(x)P_{l'-1}^{m-1}(x)\frac{dx}{\sqrt{1-x^2}} = \int_{-1}^{1} P_{l-2}^m(x)P_{l'-1}^{m-1}(x)$$
$$\times \frac{dx}{\sqrt{1-x^2}} + (2l-1)$$
$$\times \int_{-1}^{1} P_{l-1}^{m-1}(x)P_{l'-1}^{m-1}(x)dx. \quad \text{(B18)}$$

Then from the orthogonality relation of associated Legendre Polynomials,

$$\int_{-1}^{1} P_l^m(x)P_{l'}^m(x)dx = \frac{2}{2l+1}\frac{(l+m)!}{(l-m)!}\delta_{ll'}, \quad \text{(B19)}$$

we can see that the second integral on the right of Eq. (B18) vanishes for $l' \neq l$. Thus we have,

$$\int_{-1}^{1} P_l^m(x)P_{l'-1}^{m-1}(x)\frac{dx}{\sqrt{1-x^2}} = \int_{-1}^{1} P_{l-2}^m(x)P_{l'-1}^{m-1}(x)$$
$$\times \frac{dx}{\sqrt{1-x^2}}. \quad \text{(B20)}$$

We can use the above equation iteratively since the lower indices of the P_l^m's will never match as $l' > l$. So the lower index of the first polynomial in the integration can be reduced to either m or $m + 1$ (depending on $l - m$ is even or odd) by repeated use of the above identity. Thus we may write

$$\int_{-1}^{1} P_l^m(x)P_{l'-1}^{m-1}(x)\frac{dx}{\sqrt{1-x^2}}$$
$$= \begin{cases} \int_{-1}^{1} P_m^m(x)P_{l'-1}^{m-1}(x)\frac{dx}{\sqrt{1-x^2}} \\ \text{or} \\ \int_{-1}^{1} P_{m+1}^m(x)P_{l'-1}^{m-1}(x)\frac{dx}{\sqrt{1-x^2}}. \end{cases} \quad \text{(B21)}$$

Finally using the relations,

$$P_m^m = (-1)^m(2m-1)!!(1-x^2)^{m/2}$$
$$= (-1)(2m-1)\sqrt{1-x^2}P_{m-1}^{m-1}, \quad \text{(B22)}$$

$$P_{m+1}^m = x(2m+1)P_m^m$$
$$= x(2m+1)(-1)(2m-1)\sqrt{1-x^2}P_{m-1}^{m-1}$$
$$= (-1)(2m+1)\sqrt{1-x^2}P_m^{m-1}, \quad \text{(B23)}$$

and the orthonormality condition in Eq. (B2) we can see that in both the cases right side of Eq. (B21) is zero. This completes the proof.

[1] W. Hu and S. Dodelson, Annu. Rev. Astron. Astrophys. **40**, 171 (2002).

[2] J. R. Bond, C. R. Contaldi, and D. Pogosyan, Philos. Trans. R. Soc. London A **361**, 2435 (2003).

[3] F. Bouchet, astro-ph/0401108.

[4] G. Efstathiou, Mon. Not. R. Astron. Soc. **349**, 603 (2004).

[5] K. M. Gorski, Astrophys. J. Lett. **430**, L85 (1994).

[6] K. M. Gorski *et al.*, Astrophys. J. Lett. **430**, L89 (1994).

[7] K. M. Gorski *et al.*, Astrophys. J. Lett. **464**, L11 (1996).

[8] K. M. Gorski, astro-ph/9701191.

[9] M. Tegmark, Phys. Rev. D **55**, 5895 (1997).

[10] J. R. Bond, A. H. Jaffe and L. Knox, Phys. Rev. D **57**, 2117 (1998).

[11] J. Borrill, Phys. Rev. D **59**, 27302 (1999); J. Borrill, astro-ph/9911389.

[12] J. R. Bond, R. G. Crittenden, A. H. Jaffe, and L. Knox, Comput. Sci. Eng. **1**, 21 (1999).

[13] S. P. Oh, D. N. Spergel, and G. Hinshaw, Astrophys. J. **510**, 551, (1999).

[14] O. Dore, L. Knox, and A. Peel, Phys. Rev. D **64**, 083001 (2001).

[15] U. L. Pen, Mon. Not. R. Astron. Soc., **346**, 619 (2001).

[16] A. D. Challinor *et al.*, Mon. Not. R. Astron. Soc. **331**, 994 (2002); F. van Leeuwen *et al.*, Mon. Not. R. Astron. Soc. **331**, 975 (2002).

[17] B. D. Wandelt and F. Hansen, Phys. Rev. D **67**, 23001 (2003).

[18] B. D. Wandelt, D. L. Larson, and A. Lakshminarayanan, astro-ph/0310080.

[19] B. D. Wandelt, astro-ph/0401623.

[20] J. Jewell, S. Levin, and C. H. Anderson, astro-ph/0209560.

[21] J. T. Yu and P. J. E. Peebles, Astrophys. J. **158**, 103 (1969).

[22] P. J. E. Peebles, Astrophys. J. **185**, 413 (1973).

[23] B. Wandelt, E. Hivon, and K. M. Gorski, Phys. Rev. D **64**, 083003 (2003).

[24] I. Szapudi, S. Prunet, D. Pogosyan, A. Szalay, and J. R. Bond, Astrophys. J. **548**, L115 (2001).

[25] I. Szapudi, S. Prunet, and S. Colombi, Astrophys. J. **561**, L11 (2001).

[26] C. L. Bennett *et al.*, Astrophys. J. Suppl. Ser. **148**, 1 (2003).

[27] G. Hinshaw *et al.*, Astrophys. J. Suppl. Ser. **148**, 135 (2003).

[28] G. F. Smoot *et al.*, Astrophys. J. Lett. **396**, L1 (1992).

[29] E. Torbet *et al.*, Astrophys. J. **521**, L79 (1999);A. D. Miller *et al.*, Astrophys. J. **524**, L1 (1999).

[30] S. Padin *et al.*, Astrophys. J. Lett. **549**, L1 (2001).

[31] T. J. Pearson *et al.*, Astrophys. J. **591**, 556 (2003).

[32] C. L. Kuo *et al.*, Astrophys. J. **600**, 32 (2004).

[33] P. de Bernardis *et al.*, Nature (London) **404**, 955 (2000).

[34] S. Hanany *et al.*, Astrophys. J. Lett. **545**, L5 (2000).

[35] A. T. Lee *et al.*, Astrophys. J. **561**, L1 (2001).

[36] A. Benoit *et al.*, Astron. Astrophys.. **399**, L19 (2003).

[37] E. Hivon, K. M. Gorski, C. B. Netterfield, B. P. Crill, S. Prunet, and F. Hansen, Astrophys. J. **567**, 2 (2002).

[38] B. D. Wandelt and K. M. Gorski, Phys. Rev. D **63**, 123002 (2001).

[39] J. H. P. Whu *et al.*, Astrophys. J. Suppl. Ser. **132**, 1 (2001).

[40] M. Tristram, J.-C. Hamilton, J. F. Macias-Perez, and C. Renault, Phys. Rev. D **69**, 123008 (2004).

[41] T. Souradeep and B. Ratra, Astrophys. J.**560**, 28 (2001)

[42] P. Fosalba, O. Dor, and F. R. Bouchet, Phys. Rev. D **65**, 063003 (2002).

[43] K. Coble *et al.*, Astrophys. J. **584**, 585 (2003); P. Mukherjee *et al.*, Astrophys. J. **592**, 692 (2003).

[44] A. Challinor, (private communication).

[45] D. A. Varshalovich, A. N. Moskalev, and V. K. Khersonskii, *Quantum theory of angular momentum* (World Scientific, Singapore,1988).

[46] Legacy Archive for Microwave Background Data Analysis (LAMBDA), http://lambda.gsfc.nasa.gov/

[47] L. Knox, Phys. Rev. D **52**, 4307 (1995).

[48] J. R. Bond, in *Cosmology and Large Scale Structure*, Proceedings of the Les Houches Summer School, Session LX, edited by R. Schaeffer (Elsevier Science Press, New York, 1996).

[49] A. Hajian and T. Souradeep, Astrophys. J. **597**, L5 (2003); A. Hajian, T. Souradeep, and N. Cornish, astro-ph/0406354.

[50] J. M. Kovac *et al.*, Nature (London) **420**, 772 (2002).

[51] A. Kogut *et al.*, Astrophys. J. Suppl. Ser., **148**, 161 (2003).

[52] L. Page *et al.*, Astrophys. J. Suppl. Ser. **148**, 39 (2003).

[53] R. I. Jedrzejewski, Mon. Not. R. Astron. Soc. **226**, 747 (1987).

[54] George B. Arfken and Hans J. Weber, *Mathematical Methods for Physicists*, (Academic Press, San Diego, 2001).